






Characterization of Bio-Optical Anomalies in the Kerguelen Region, Southern Indian Ocean: A Study Based on Shipborne Sampling and BioGeoChemical-Argo Profiling Floats

J. Uitz¹ , C. Roesler², E. Organelli³ , H. Claustre¹, C. Penkerch¹, S. Drapeau², E. Leymarie¹, A. Poteau¹, C. Schmechtig⁴, C. Dimier⁵ , J. Ras¹, X. Xing⁶ , and S. Blain⁷ 

¹Laboratoire d'Océanographie de Villefranche (LOV), UMR 7093, CNRS and Sorbonne Université, Villefranche-sur-Mer, France, ²Earth and Oceanographic Science, Bowdoin College, Brunswick, ME, USA, ³National Research Council (CNR), Institute of Marine Sciences (ISMAR), Rome, Italy, ⁴OSU Ecce Terra, UMS 3455, CNRS and Sorbonne Université, Paris Cedex, France, ⁵CNRS and Sorbonne Université, Institut de la Mer de Villefranche (IMEV), Villefranche-sur-Mer, France, ⁶State Key Laboratory of Satellite Ocean Environment Dynamics (SOED), Second Institute of Oceanography, Ministry of Natural Resources, Hangzhou, China, ⁷Laboratoire d'Océanographie Microbienne (LOMIC), UMR 7621, CNRS and Sorbonne Université, Banyuls-sur-Mer, France

Key Points:

- Contribution by large diatoms and photoacclimation are major drivers of a negative anomaly in the blue chlorophyll-specific phytoplankton absorption coefficient
- BioGeoChemical-Argo observations indicate a bio-optical anomaly exists over the entire year with maximal values associated with seasonal blooms
- The Indian Southern Ocean shows a large seasonal and regional variability in bio-optical regimes that lie outside the global means

Supporting Information:

Supporting Information may be found in the online version of this article.

Correspondence to:

J. Uitz,
julia.uitz@imev-mer.fr

Citation:

Uitz, J., Roesler, C., Organelli, E., Claustre, H., Penkerch, C., Drapeau, S., et al. (2023). Characterization of bio-optical anomalies in the Kerguelen region, Southern Indian Ocean: A study based on shipborne sampling and BioGeoChemical-Argo profiling floats. *Journal of Geophysical Research: Oceans*, 128, e2023JC019671. <https://doi.org/10.1029/2023JC019671>

Received 26 JAN 2023

Accepted 2 NOV 2023

Abstract The Southern Ocean (SO) is known for its atypical bio-optical regime. This complicates the interpretation of proxies measured from satellite and in situ platforms equipped with optical sensors, which occupy an important niche for monitoring the vast and remote SO. A ship-based field study in concert with time series observations from BioGeoChemical-Argo (BGC-Argo) profiling floats were used to investigate spatial and temporal variations in bio-optical relationships in the open ocean waters surrounding the Kerguelen Plateau in the Indian sector of the SO. Compared to other regions with similar chlorophyll concentrations, chlorophyll-specific phytoplankton absorption in the blue waveband presented a consistent negative anomaly. The anomaly was uniform over deep mixed layers and correlated with phytoplankton size, photoacclimation and atypically high concentrations of fucoxanthin. The BGC-Argo observation-based proxies revealed that the blue absorption anomaly increased with chlorophyll concentration both spatially and temporally and, while particularly pronounced in the naturally iron-fertilized waters, was also found in the High Nutrient Low Chlorophyll region. While phytoplankton size was an important driver of the anomaly, photoacclimation associated with self-shading of phytoplankton cells was also involved during intense blooms. The backscattering coefficient exhibited negative and positive anomalies in the low and high biomass regimes, respectively. The large positive anomaly in high biomass regimes was attributed to the variable non-algal particles characteristics associated with a relatively high production of bloom by-products. With clear understanding of the bio-optical anomalies, BGC-Argo floats stand as unique tools for monitoring the bio-optical spatio-temporal complexity of the SO.

Plain Language Summary The Southern Ocean (SO) plays a key role in Earth's climate. However, its remoteness and harsh climate necessitate remote sensing approaches such as optical sensors on profiling floats and satellites. These require optical measurements and shipboard samples to relate optical signals to biological properties, called optical proxies. The SO optical proxies have been found to be very different from those measured in other oceanic regions. Here the proxies in the Kerguelen region are investigated along a ship's track crossing from subtropical to subpolar latitudes. The Kerguelen Plateau impedes both wind and currents such that deep waters upwell to the surface providing nutrients to primary producers. This region in the Indian sector of the SO provides a tremendous range in ecosystem properties from nutrient-starved to nutrient-rich, making these results applicable to other SO areas. The authors find that the differences in optical proxies can be explained by the presence of different phytoplankton communities and their responses to being mixed to depths where light is limited. This explains why the proxies vary so significantly across this region and change over the seasons. This knowledge makes the observations obtained by floats and satellites invaluable for understanding the entire SO.

1. Introduction

The Southern Ocean (SO) plays a critical role in the Earth's climate system. It exchanges and redistributes seawater properties (salt, nutrients, heat, gases) to other ocean basins and sequesters large amounts of carbon, which

© 2023. The Authors.

This is an open access article under the terms of the [Creative Commons Attribution-NonCommercial-NoDerivs License](https://creativecommons.org/licenses/by-nc-nd/4.0/), which permits use and distribution in any medium, provided the original work is properly cited, the use is non-commercial and no modifications or adaptations are made.

makes the SO a major sink for atmospheric CO₂ (Frölicher et al., 2015; Sabine et al., 2004; Takahashi et al., 2012) through the solubility and biological pumps, the former being dominant (Gruber et al., 2019). The intensity of the SO carbon sink has been observed to change over interannual to decadal timescales (Gruber et al., 2019; Landschützer et al., 2015; Le Quéré et al., 2010), but the time course of variations and underlying mechanisms are difficult to monitor and quantify (Bushinsky et al., 2019; Lovenduski et al., 2015).

Ongoing climate change will, and does already, result in major modifications of the SO environmental conditions. Observed changes in the properties of SO water masses include significant warming of the upper 1,000 m, particularly within the 40°S–65°S latitudinal band (Gille, 2002; Sallée, 2018) and freshening of intermediate waters (Wong et al., 1999; Yao et al., 2017) as well as recent variability in salinity of bottom water (Aoki et al., 2020; Rintoul, 2007) and acidification (Jiang et al., 2023). The prevailing westerly and polar easterly wind bands, responding to increases in atmospheric CO₂ and decreasing stratospheric ozone, have undergone both a poleward shift and intensification (Goyal et al., 2021; Polvani et al., 2011; Shindell & Schmidt, 2004). Changing SO winds may alter the deep overturning circulation and water column stratification in ways that are as yet unclear (Böning et al., 2008; Meijers, 2014; Rintoul, 2018; Stewart & Thompson, 2012). That said, the SO does show the most significant trends in both strengthening stratification and deepening summertime mixed layers (Sallée et al., 2021), impacting both the light and nutrient environment for primary producers (e.g., Boyd et al., 2008; Deppeler & Davidson, 2017; Henley et al., 2020).

All of these changes will undoubtedly alter the strength of the SO carbon sink and the ecosystem functioning in a way that is difficult to predict (Frölicher et al., 2015, 2016; Kwiatkowski et al., 2020). Although often described as the largest High Nutrient Low Chlorophyll (HNLC) zone of the world ocean, the SO hosts a variety of other biogeochemical regimes (Ardyna et al., 2017; Leung et al., 2015; Sallée et al., 2015; Thomalla et al., 2011), making it a complex system driven by the interplay of several environmental factors, that is, not only iron but also light, silicic acid, manganese, or grazing (e.g., Blain et al., 2007; Boyd, 2002; Browning et al., 2021; Mitchell et al., 1991; Strzepek et al., 2012; Trimborn et al., 2019).

In spite of this key role, the SO remains poorly studied with many gaps in understanding because of its remoteness and harsh weather conditions. These constraints lend themselves to the use of remote platforms for improved temporal and spatial observations. In this context, both autonomous satellite-based and floating/profiling observation platforms equipped with optical sensors can contribute meaningfully to our goal of achieving a more complete understanding of the SO ecosystems. To be useful, optical observations must be interpreted in the context of biogeochemical properties, requiring robust proxies. However, biogeochemical interpretation of optical proxies can be complicated, necessitating focused and local quantification of bio-optical relationships. Logistical constraints have resulted in a body of literature on the optical properties essentially dedicated to the polar southern waters in near-coastal areas (e.g., Antarctic Peninsula, Patagonian Shelf, southern Ross Sea), which are unlikely to be representative of the broad range of biogeochemical regimes observed in the entire SO (e.g., Ardyna et al., 2017; Thomalla et al., 2011) and which leaves the subpolar SO generally undersampled (Robinson et al., 2021).

Previous studies conducted in the SO suggest an atypical bio-optical regime compared to low-latitude regions (e.g., Reynolds et al., 2015 and references herein) with particularly low values of the particulate absorption coefficient (a_p), generally attributed to a reduced contribution to absorption by both the phytoplankton (a_{ph}) and non-algal components (a_{NAP}) (Mitchell, 1992; Mitchell & Holm-Hansen, 1991a; Sosik et al., 1992). More importantly is the observation that each of these values is lower than expected for a given chlorophyll concentration compared to other regions. Reduction of the chlorophyll-specific phytoplankton absorption coefficient and flattening of the spectra are thought to be associated with an enhanced package effect associated with large phytoplankton cells and/or photoacclimation in response to chronic low light levels encountered in the SO (Dierssen & Smith, 2000; Mitchell & Holm-Hansen, 1991a; Sosik et al., 1992). This apparent bio-optical anomaly is thought to lead to underestimation of the chlorophyll concentration derived from global satellite ocean color algorithms (Dierssen & Smith, 2000; Garcia et al., 2005; Hirawake et al., 2000; Johnson et al., 2013; Szeto et al., 2011), although recent evidence challenges this view (Haëntjens et al., 2017; Moutier et al., 2019). Yet the picture may be more complex as the spectral phytoplankton absorption coefficient shows large regional variability, with major differences associated with phytoplankton composition (Arrigo et al., 1998; Brody et al., 1992; Ferreira et al., 2017; Figueroa, 2002) as well as physiological status (e.g., Halsey & Jones, 2015; Uitz et al., 2008).

A critical step for establishing robust optical proxies for biogeochemical variables is to move from extrinsic proxies (i.e., those based on covariations rather than causal relationships) to intrinsic proxies (i.e., based on causal relationships, relying on constitutional properties). Most of the commonly implemented proxies are based upon

extrinsic relationships that are largely driven by the covariability of materials in the ocean, such as chlorophyll or particulate organic carbon, over multiple orders of magnitude in variation. Although relationships are observed over the global orders of magnitude range, significant variations are typically observed about these relationships (e.g., the scatter in the relationship between the backscattering coefficient and chlorophyll concentration). The variability in these extrinsic relationships can be better assessed using *intrinsic* proxy relationships that attempt to remove the effects of concentration. Intrinsic relationships such as spectral ratios and spectral slopes of optical properties reveal composition, size distribution, physiological status, making them more robust proxies for biogeochemical properties rather than just concentration.

The aim of this work is to test the hypothesis that the SO is broadly characterized by a negative bio-optical anomaly, a conclusion that is largely driven by observations collected in the coastal and marginal sea ice zones and during peak phytoplankton blooms. We start with examining extrinsic relationships (e.g., a_{ph} vs. chlorophyll) to identify the anomaly, and then delve into intrinsic relationships (e.g., $a_{ph}(440)/a_{ph}(676)$ versus chlorophyll) to investigate the sources of the anomaly. Near-surface ocean relationships are highlighted for application to satellite ocean color remote sensing, while variations with depth through the mixed layer and euphotic zone reveal how representative the surface is. The study focuses on the optical properties of the region explored during the “Southern Ocean and CLIMate: field studies with innovative tools” (SOCLIM) cruise, conducted in the Indian Sector of the SO in the vicinity of the Kerguelen Island. The region is selected to provide a broad range of bio-optical regimes from the transition across oligotrophic subtropical gyre to the subpolar waters of the SO that include naturally Fe-enriched waters on the Kerguelen Plateau (KP) to HNLC conditions and the seasonal sea ice zone (Blain et al., 2007, 2013; Rembauville et al., 2017). This data set presents a twofold interest. First, this region is poorly documented in bio-optical data and presents large gradients in algal and non-algal materials. Second, to our knowledge, the present data set is unique for two reasons. It comprises measurements of the light absorption coefficients, not only of the algal and non-algal components, but also of colored dissolved organic matter, which has rarely been measured in the SO (Ferreira et al., 2018), and may represent an important component of the bio-optical status of a given water body. It also comprises, in addition to in situ measurements of optical coefficients (absorption, backscattering), phytoplankton pigment determinations, as well as enumeration and taxonomic identification of phytoplankton cells from flow cytometry and inverted microscopy, which is scarcely the case in bio-optical studies.

The field cruise measurements are complemented with an in situ data set collected by BioGeoChemical-Argo (BGC-Argo) profiling floats. These measurements, and derived optical proxies, enable the investigation of the regional and seasonal variability in the bio-optical relationships and anomalies that would not be permitted by the sole field cruise data set. Importantly, the BGC-Argo data set enables us to examine the bio-optical status of the study region and beyond in the winter, when no field data have been collected thus far.

In brief, the study presented here aims at: (a) Documenting the bio-optical properties of southern subpolar open waters, which are relatively undersampled compared to polar near-coastal waters from a bio-optical perspective; (b) Examining the bio-optical relationships to determine whether they are atypical and discuss potential sources; (c) Using proxies derived from BGC-Argo data to investigate the regional and seasonal variability in the bio-optical relationships.

2. Data and Methods

2.1. Study Region

The present study makes use of an in situ data set collected during the SOCLIM field cruise (<https://doi.org/10.17600/16003300>). The cruise was conducted onboard R/V Marion Dufresne II from 5 October to 1 November 2016, in the Indian Sector of the SO, with a specific focus on the Kerguelen Island area. The SOCLIM cruise covered a large transect from $\sim 25^{\circ}\text{S}$ to $\sim 60^{\circ}\text{S}$, spanning a broad range of biogeochemical and bio-optical regimes (Figure 1a), including the oligotrophic conditions of the subtropical Southern Indian Ocean, the HNLC conditions upstream of the Kerguelen Island, and the iron-enriched eutrophic conditions above the KP. SOCLIM visited 12 sampling stations (Figure 1a), with station A3 visited twice, 6 days apart (A3_1 and A3_2).

In addition to the SOCLIM data set, the present study utilizes measurements acquired by 16 BGC-Argo profiling floats deployed in the framework of distinct projects in the study area, at three biogeochemically distinct locations: HNLC conditions (station FS), Kerguelen iron-enriched conditions (stations A3 and TNS-06), and

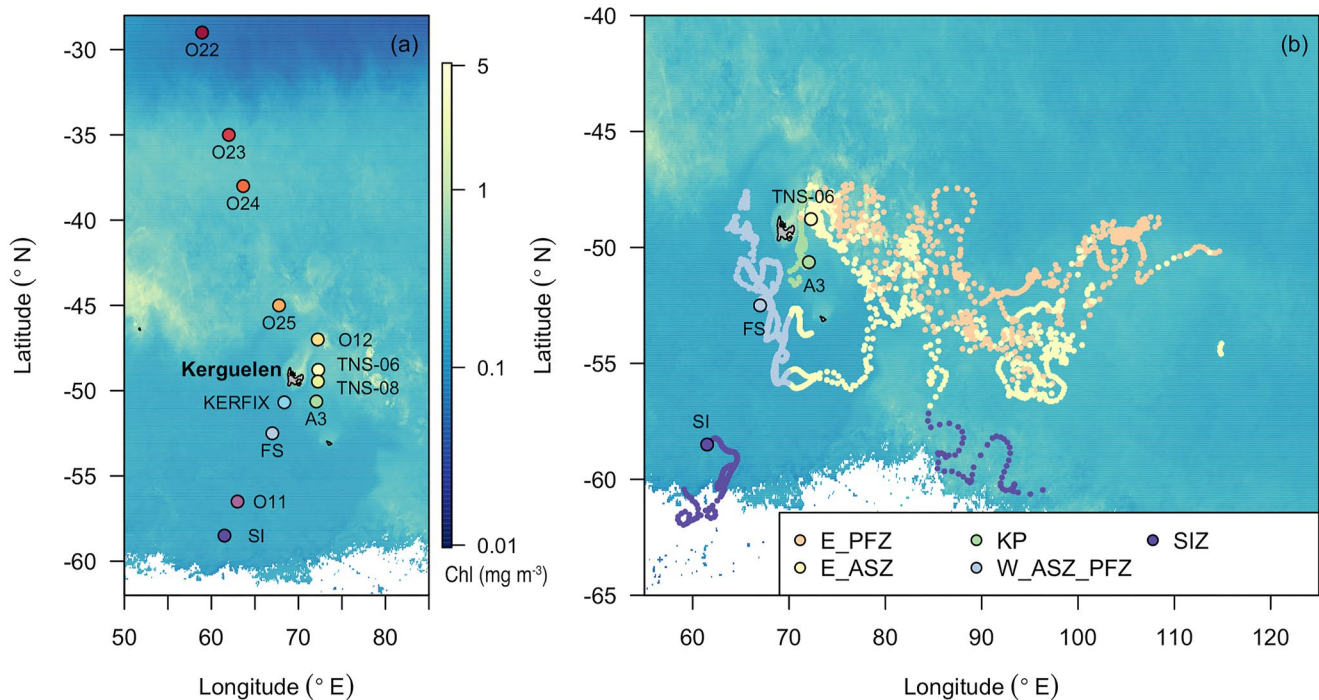


Figure 1. Geographic location of (a) the SOCLIM cruise sampling stations and (b) the trajectories of the BGC-Argo floats with the main SOCLIM stations. In panel (a) the color code of the sampling stations follows a north-south gradient (from warm color in the subtropics to cold color in the seasonal ice region); in panel (b) the color code indicates the zone in which the BGC-Argo data were collected from north to south: East Polar Front Zone (E_PFZ), East Antarctic Southern Zone (E_ASZ), Kerguelen Plateau, West Polar Front Zone, and West Antarctic Southern Zone (W_PFZ_ASZ), and Seasonal Ice Zone. For both maps, the surface chlorophyll concentration (in mg m^{-3}) derived from a MODIS mission composite for the month of October is used as a background.

seasonal sea-ice area (SI). The trajectories of the BGC-Argo floats are shown in Figure 1b while complementary information on float deployments and related projects is provided in Table 1.

2.2. Shipborne Measurements From the SOCLIM Cruise

2.2.1. Particulate Organic Carbon and Phytoplankton Pigments

Seawater for the analysis of the particulate organic carbon concentration (POC) and phytoplankton pigments was sampled from Niskin bottles mounted on a CTD-rosette device, at 12 depths (from the surface to 1,000 m for POC and 500 m for pigments) at each of the 12 SOCLIM stations. Approximately 2 L of seawater were filtered onto Whatman GF/F filters (0.7 μm pore size, 25 mm diameter), using pre-combusted filters for POC samples. POC determinations were performed as described in Rembauville et al. (2017). In brief, the filter samples were stored into pre-calcinated glass vials, oven-dried and stored until post-cruise analysis in the laboratory. Prior to analysis, the filters were fumigated with HCl. Analyses were performed using a CHN analyzer (Perkin-Elmer 2400). The POC data were not corrected for possible adsorption of dissolved organic carbon on the filters, which could lead to an overestimation of the POC values (Cetinić et al., 2012; Moutier et al., 2019 and references herein). However, the POC values presented here are simply used qualitatively as an indicator of the total biomass with no impact on our analysis. Thus, for the sake of consistency, we kept the values presented in Rembauville et al. (2017).

For phytoplankton pigment determination, samples were flash-frozen in liquid nitrogen immediately after filtration and stored at -80°C until transport to the laboratory in liquid-nitrogen dry shippers. Filters were extracted in 3 mL of pure methanol at -20°C for 1 hr. The extracts were vacuum-filtered through GF/F filters and then analyzed (within 24 hr) by HPLC using a complete Agilent Technologies system. The protocol of Ras et al. (2008) was used to separate and quantify a suite of 26 pigments, including chlorophyll *a* (Chla) and divinyl-chlorophyll *a* (DVChla), the sum of the concentrations of which is referred to as total chlorophyll *a* (TChla) and is an indicator of the phytoplankton biomass. These also include a variety of accessory pigments, among which some that can be used as biomarkers of phytoplankton taxonomic groups (Jeffrey et al., 1997), such as fucoxanthin (Fuco), peridinin

Table 1
BioGeoChemical-Argo Float WMO and Deployment Information

WMO	Project	Cruise	Zone	Station	Date
6901574	remOcean	OISO	W_PFZ_ASZ	FS (BA1)	01.20.2015
6901579	remOcean	OISO	W_PFZ_ASZ	FS (BA1)	01.20.2015
6901581	remOcean	OISO	KP	A3	01.21.2015
6901689	remOcean	OISO	KP	A3	01.21.2015
6901580	remOcean	OISO	KP	TNS-06 (E)	01.24.2015
6901004	remOcean	OISO	KP	TNS-06 (E)	01.24.2015
6902738	SOCLIM	SOCLIM	KP	TNS-06	10.16.2016
6902734	SOCLIM	SOCLIM	KP	TNS-06	10.16.2016
6902736	SOCLIM	SOCLIM	KP	A3_1	10.18.2016
6902737	SOCLIM	SOCLIM	KP	A3_1	10.18.2016
6902735	SOCLIM	SOCLIM	W_PFZ_ASZ	FS	10.19.2016
6902739	SOCLIM	SOCLIM	W_PFZ_ASZ	FS	10.19.2016
6902742	SOCLIM	SOCLIM	SIZ	SI	10.21.2016
6902743	SOCLIM	SOCLIM	SIZ	SI	10.21.2016
6902880	SIDONI	MOBYDICK	W_PFZ_ASZ	FS (M4_1)	03.02.2018
6902905	SIDONI	OISO	W_PFZ_ASZ	FS (M4_1)	01.25.2019

Note. The station labels indicated between brackets are the actual labels of the deployment cruise which correspond to the SOCLIM stations labels.

(Peri), 19'-hexanoyloxyfycoxanthin (Hex), 19'-butanoyloxyfycoxanthin (But), alloxanthin (Allo), total chlorophyll *b* (TChlb, the sum of monovinyl- plus divinyl-chlorophyll *b*), zeaxanthin (Zea), and prasinoxanthin (Pras).

The concentration of non-photosynthetic carotenoids (NPC) is calculated as the sum of the concentrations of Zea, Allo, alpha-, and beta-carotenes, diadinoxanthin and diatoxanthin, whereas the concentration of the major photosynthetic pigments (PAP) is calculated as the sum of the concentrations of TChlb and chlorophyll *c* (TChlc, the sum of chlorophyll *c*1, *c*2, and *c*3), Fuco, Peri, Hex, and But. The total accessory pigment (TAP) concentration is defined as the sum of NPC and PAP. Finally, the pigment composition for each sample was scaled to the TChla concentration and a hierarchical cluster analysis was performed following the approach of Kramer and Siegel (2019) and making use of the code generously provided by S. Kramer on github (<https://github.com/sashajane19/HPLCcluster>).

2.2.2. Size of the Phytoplankton Community

We estimate the average size of the phytoplankton community using two different indices. The first one is the pigment-derived size index (SI) of Bricaud et al. (2004) calculated as:

$$SI = f_{\text{pico}} \times 1 + f_{\text{nano}} \times 5 + f_{\text{micro}} \times 50 \quad (1)$$

where f_{pico} , f_{nano} , and f_{micro} are, respectively, the relative contribution to the TChla concentration of the pico-, nano-, and microphytoplankton size classes, derived from the pigment concentrations as in Uitz et al. (2006). The values 1, 5, and 50 are approximate mean values of cell size (in μm) for the pico-, nano-, and microphytoplankton size classes, respectively. Because the mean values selected by Bricaud et al. (2004) are not necessarily adequate for the study area, we use a normalized index calculated as the ratio of SI to the maximum value for the data set (i.e., 50 μm), SI_{norm} . For comparison with previous studies (e.g., Bricaud et al., 2004; Uitz et al., 2015), we note that the non-normalized SI index varies between 10 and 50 μm .

The second size indice was calculated from phytoplankton morphological measurements performed by Rembauville et al. (2017). Essentially, the equivalent spherical diameter (ESD) and cellular abundance were determined at 10 stations (the 12 sampling stations except O22 and O24) and 3 depths (10, 100, and 250 m) using flow cytometry for the pico- and nanophytoplankton size classes and inverted microscopy applied to Lugol-fixed

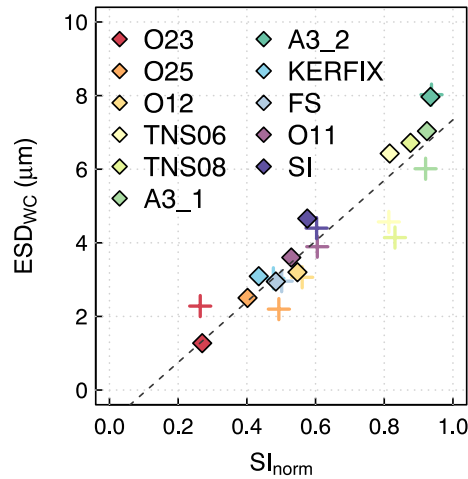


Figure 2. Comparison of the mean community weighted equivalent spherical diameter (ESD_{CW}) determined from microscopy and flow cytometry enumerations (in μm) and the pigment-based normalized size index (SI_{norm}). The color code indicates the SOCLIM cruise sampling stations and the symbols the depth of acquisition. Values within the layer 0–150 m are shown, with surface data represented by the diamond symbols.

samples for the microphytoplankton class (lower size limit of $\sim 5 \mu\text{m}$). For each sampled depth and station, we calculated a community weighted ESD (ESD_{CW}) defined as:

$$ESD_{CW} = \sum_i (N_i ESD_i) / N_{tot} \quad (2)$$

with N_i the cellular abundance of a given phytoplankton taxon “ i ”, ESD_i the ESD of this taxon (in μm), N_{tot} the total number of phytoplankton cells of all considered taxa. For pico- and nanophytoplankton taxa, N_i is provided from flow cytometry analyses and ESD_i assumed to be $0.6 \mu\text{m}$ for *Prochlorococcus*, $1 \mu\text{m}$ for *Synechococcus* and picoeukaryotes, and $5 \mu\text{m}$ for nanoeukaryotes. For microphytoplankton, both N_i and ESD_i are given by inverted microscopy analyses. The reader is referred to Rembauville et al. (2017) for further details. The SI_{norm} index is strongly correlated with ESD_{CW} (Figure 2; $r^2 = 0.84$, $n = 22$, $p < 0.001$), suggesting it is a robust proxy of the variability in the average size of the phytoplankton assemblage.

2.2.3. Particulate, Phytoplankton and Non-Algal Spectral Absorption Coefficients

The spectral absorption coefficients of particles, $a_p(\lambda)$, were determined using the same seawater sample filters as those used for the HPLC pigment analyses, following IOCCG protocols (Roesler et al., 2018). The $a_p(\lambda)$ spectra were measured directly on the filters with a Lambda 19 spectrophotometer

(Perkin Elmer) equipped with an integrating sphere (Labsphere), with the filters placed inside the sphere. A blank wet GF/F filter was used as the baseline. The measured optical density (OD) values were corrected for the baseline and pathlength amplification effect according to the procedure of Stramski et al. (2015). The corrected OD values were then converted into $a_p(\lambda)$. The numerical method of Bricaud and Stramski (1990) was thereafter used to partition the $a_p(\lambda)$ values into absorption by phytoplankton, $a_{ph}(\lambda)$, and non-algal particles, $a_{NAP}(\lambda)$.

The robustness of the Bricaud and Stramski (1990) numerical method for application to the present data set was assessed. For 9 of the 12 stations, we collected additional seawater samples from the surface flow-through system of the vessel. The filters were scanned with the spectrophotometer to measure $a_p(\lambda)$ and rescanned after chemical extraction of pigments in pure methanol (Kishino et al., 1985) to measure $a_{NAP}(\lambda)$, $a_{ph}(\lambda)$ being calculated as the difference $a_p(\lambda) - a_{NAP}(\lambda)$. Finally, the $a_{ph}(\lambda)$ values retrieved from the numerical method applied to the $a_p(\lambda)$ measurements were compared to the $a_{ph}(\lambda)$ values obtained after the chemical extraction as the reference. The average error is 3.6% and 0% for $a_{ph}(440)$ and $a_{ph}(676)$, respectively (Figure 3). The exponential spectral slope of the measured $a_{NAP}(\lambda)$, S_{NAP} , was computed for each of the measured spectra by non-linear least-squares regression over the wavelength range 400–700 nm (Roesler et al., 1989):

$$a_{NAP}(\lambda) = a_{NAP}(440) \times e^{-S_{NAP}(\lambda-440)} \quad (3)$$

For comparison purposes, we also use the method of Roesler et al. (1989) for retrieving the $a_{ph}(\lambda)$ and $a_{NAP}(\lambda)$ coefficients from the measured $a_p(\lambda)$ spectra. The two methods of Bricaud and Stramski (1990) and Roesler et al. (1989) converge and yield minor differences in the retrieved absorption coefficients (not shown). In addition, both methods provide unrealistic values of $a_{NAP}(440)$ and S_{NAP} for both visits of station A3, which we therefore ignore in our analysis. We suggest this may be the consequence of the shallow bathymetry of station A3 ($\sim 530 \text{ m}$) accompanied by large amounts of suspended lithogenic material for which the numeric deconvolution methods have not been calibrated.

2.2.4. Colored Dissolved Organic Matter Spectral Absorption Coefficient

The spectral absorption coefficient of colored dissolved organic matter (CDOM), $a_{CDOM}(\lambda)$, was determined following the protocol described in Bricaud et al. (2010). Essentially, at each station seawater samples were collected from Niskin bottles at 12 depths (surface to 1,000 m) into 250-mL dark brown glass bottles. Each seawater sample was filtered onto a polycarbonate membrane ($0.2 \mu\text{m}$ pore size, 47 mm diameter) previously rinsed with milli-Q water and the filtrate was collected into a 250-mL dark brown glass bottle, which was prepared by soaking into 5% detergent (Decon 90) and 10% HCl, with milli-Q water rinses before, between and after.

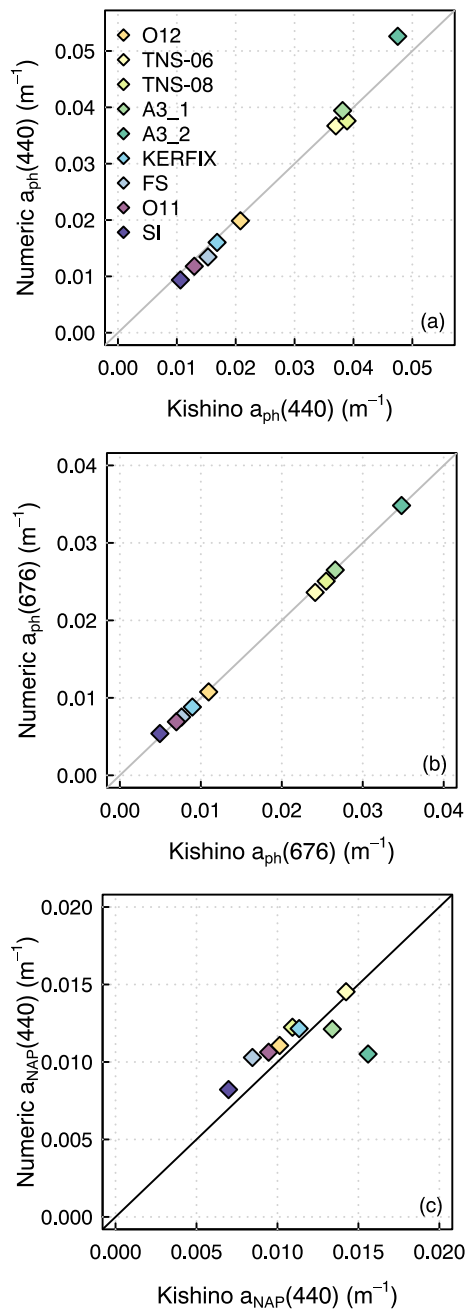


Figure 3. Comparison of the spectral absorption coefficients of (a) phytoplankton at 440 nm, $a_{ph}(440)$, and (b) 676 nm, $a_{ph}(676)$, and of (c) non-algal particles at 440 nm, $a_{NAP}(440)$, derived from a numerical deconvolution method and the Kishino et al. (1985) chemical extraction method for surface seawater samples collected at nine stations, as indicated by the color coding. The one-to-one line is shown for reference.

using the bio-optical relationship of Morel and Maritorena (2001). The MLD and Z_{eu} are merely presented as an indication of the biogeochemical regime in Figure 4a. In order to interpret the variability in the bio-optical properties measured during the cruise (Section 3.2), we considered separately the data collected in the surface layer, that is, <10 m deep, and in the rest of the water column. This is to be consistent with satellite remote sensing of ocean color which characterizes the oceanic surface layer and for which the issue of bio-optical relationships and anomalies is critical.

The samples were immediately analyzed onboard using an UltraPath (WPI Inc.) spectrophotometer that comprises a waveguide with an adjustable path-length set at 200 cm. Reference seawater was prepared daily for each station using milli-Q water and pre-combusted artificial salt at a concentration of 34 or 35 g L⁻¹ tuned for each station. Prior to each measurement and after each set of analyses, the UltraPath sample cell was carefully flushed using successively solutions of 5% detergent, 50% methanol, 10% HCl 10%, and milli-Q water. For an updated CDOM absorption measurement protocol, the reader is referred to the IOCCG report (Mannino et al., 2019).

The baseline-corrected OD values were converted into $a_{CDOM}(\lambda)$. As with the non-algal particle spectra, we also calculated the slope of the $a_{CDOM}(\lambda)$ spectra, S_{CDOM} , by applying a non-linear least-squares fit to the values measured within the 350–500 nm spectral range using 440 nm as the reference wavelength (Babin et al., 2003; Bricaud et al., 1981):

$$a_{CDOM}(\lambda) = a_{CDOM}(440) \times e^{-S_{CDOM}(\lambda-440)} \quad (4)$$

2.2.5. Particulate Backscattering Coefficient

The particulate backscattering coefficient at 700 nm, $b_{bp}(700)$, was measured using a WET Labs ECO Puck triplet attached to the frame of the CTD-rosette device at all stations except O24. The data processing follows the standard BGC-Argo protocol given by Schmechtig et al. (2018). The sensor raw counts were converted into the volume scattering function (VSF) at an angle of 124° and at wavelength of 700 nm, $\beta(124,700)$, by applying the sensor-specific dark value and scaling factor provided by the manufacturer. The $b_{bp}(700)$ coefficient was calculated following Boss and Pegau (2001):

$$b_{bp}(700) = \chi(124)2\pi (\beta(124, 700) - \beta_{sw}(124, 700)) \quad (5)$$

where $\chi(124)$ is the angle-dependent conversion factor equal to 1.076 (Sullivan et al., 2013), and $\beta_{sw}(124,70)$ is the salinity- and temperature-dependent contribution of pure water to the VSF computed according to Zhang and Hu (2009). The $b_{bp}(700)$ profiles values were smoothed using a five-point running median and a seven-point running mean as in Briggs et al. (2011) in order to remove spikes associated with large particles. The final $b_{bp}(700)$ values were taken as the median of the values measured at the depth (± 1 m) corresponding to the discrete seawater samples from the associated Niskin bottle.

2.2.6. Mixed, Euphotic, and Surface Layers

For each SOCLIM sampling station, we determined the mixed layer depth (MLD) using density profiles derived from the CTD measurements with an excess density criterion of 0.03 kg m⁻³ compared to the near-surface (10 m depth) value (de Boyer Montégut et al., 2004). We also determined the euphotic layer depth (Z_{eu}), defined as the depth at which the photosynthetically available radiation (PAR) reduces to 1% of its value just below the surface. Since daytime PAR measurements were not available, Z_{eu} was inferred from the vertical distribution of TChla following Morel and Berthon (1989) and

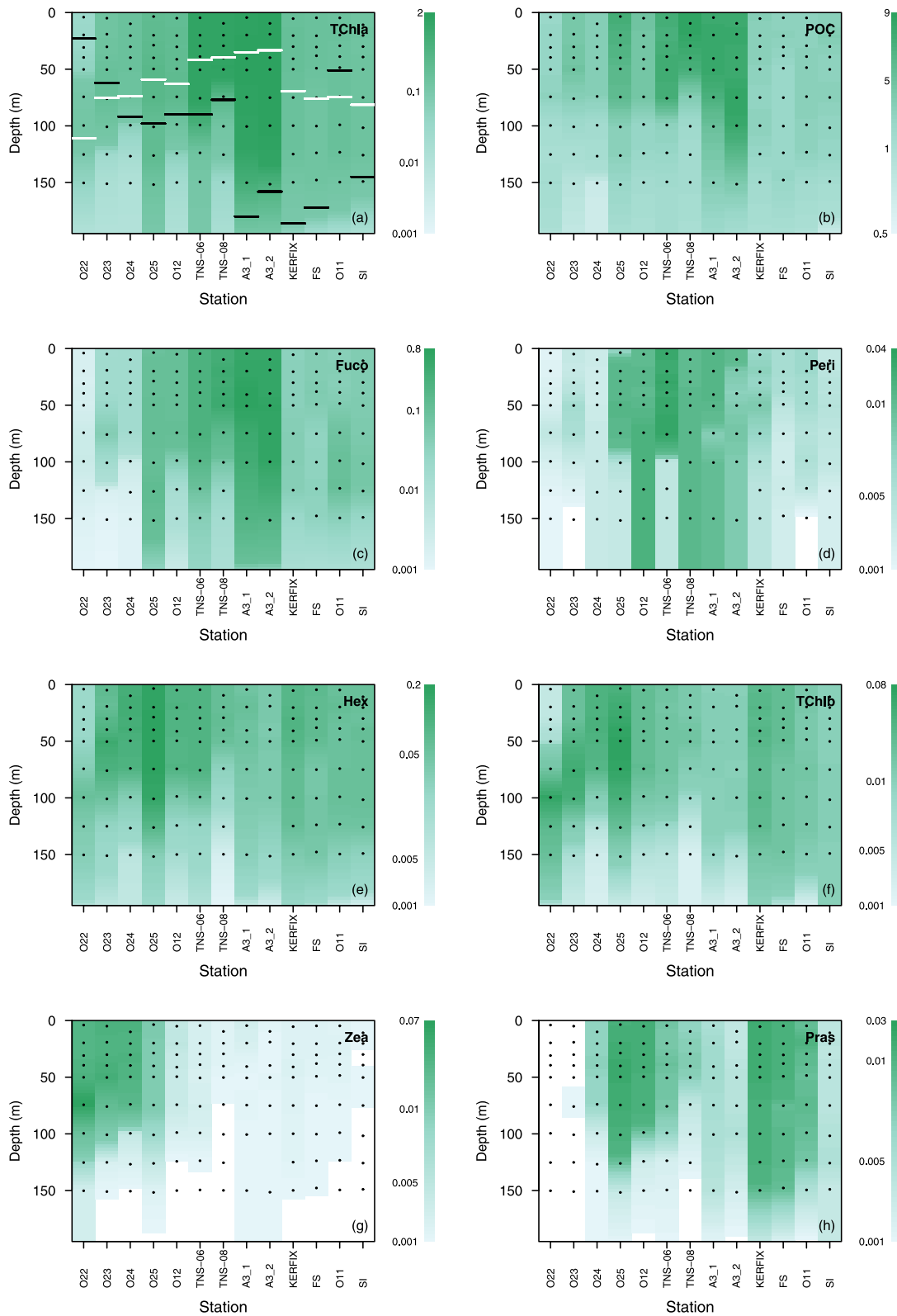


Figure 4. Vertical distribution of the concentrations of major phytoplankton pigments and particulate organic carbon along the SOCLIM cruise transect: (a) total chlorophyll *a*, TChla; (b) particulate organic carbon, POC; (c) fucoxanthin, Fucop; (d) peridinin, Peri; (e) 19'-hexanoyloxyfucoxanthin, Hex; (f) total chlorophyll *b*, TChlb; (g) zeaxanthin, Zea; and (h) prasinocanthin, Pras. All units are mg m^{-3} with the exception of POC which is $\mu\text{mol L}^{-1}$. In panel (a), the horizontal white and black bars indicate the depth of the euphotic and mixed layers, respectively.

2.3. BGC-Argo Float Data

The BGC-Argo profiling floats used in this study were all equipped with: an SBE 41 (Sea-Bird Scientific) CTD sensor; an OCR-504 (Sea-Bird Scientific) multispectral radiometer that measures the PAR and the downwelling irradiance at 380 nm, $E_d(380)$, 412 nm, $E_d(412)$, and 490 nm, $E_d(490)$; an ECO Puck triplet (Sea-Bird Scientific) that measures the fluorescence by Chla (at 470 nm/695 nm excitation/emission wavelengths) and CDOM (370 nm/460 nm), and $b_{bp}(700)$. The data acquired by the profiling floats were downloaded freely from the Coriolis Data Center. As for hydrological CTD casts, the $b_{bp}(700)$ measurements from BGC-Argo floats were processed following Schmechtig et al. (2018). The processing of the measurements of Chla fluorescence and diffuse attenuation coefficients (K_d) is described below.

2.3.1. Fluorescence-Derived Chlorophyll *a* Concentration

Following the BGC-Argo protocol (Schmechtig et al., 2015), the raw chlorophyll fluorescence counts were converted into Chla concentrations using the manufacturer-provided dark count and scaling coefficient. The calibrated fluorescence vertical profiles were adjusted for non-zero deep values and corrected for negative spikes. Non-photochemical quenching was corrected following Xing et al. (2012).

Roesler et al. (2017) studied the variability of a factor defined as the ratio between Chla concentration derived from factory-calibrated fluorescence in situ measurements from ECO sensors (WET Labs) and that determined from various methods used as the reference (HPLC, radiometry, spectrophotometry). They obtained a factor of 2 overestimation for the global ocean (recommended to be applied to any ECO sensor fluorescence measurement) and observed a broad regional variability with up to a factor of 4 overestimate for the Indian sector of the SO. This regional value is quite consistent with results from the present study. Indeed, for each BGC-Argo float presented in Table 1, we computed a linear regression model using paired values of fluorescence-derived Chla and HPLC-determined Chla from samples collected at float deployment. The obtained regression coefficients range within 0.7–6.5, with an average value of 3.1. We also calculated, for each of the considered BGC-Argo floats, the radiometry-based F_{490} factor of Xing et al. (2011), which shows values within 2.6–7.7 and an average of 3.7. Therefore, we applied, on the one hand, the global correction factor of 2 and, on the other hand, the regional correction factor of 4 in order to provide an envelope for the BGC-Argo fluorescence-derived Chla concentration.

2.3.2. Diffuse Attenuation Coefficient for Downwelling Irradiance

The BGC-Argo float measurements of spectral downwelling irradiance, $E_d(\lambda)$, were processed and quality-controlled following the method of Organelli et al. (2016) developed to derive the diffuse attenuation coefficient for E_d . Briefly, counts from the OCR-504 sensor were converted into $E_d(380)$, $E_d(412)$, and $E_d(490)$ (in units of $\mu\text{W cm}^{-2} \text{nm}^{-1}$) using channel-specific calibration coefficients provided by the manufacturer. The E_d vertical profiles acquired under very unstable sky and sea conditions were rejected. For the remaining profiles, we identified non-zero deep values. Measurements affected by sporadic clouds, wave focusing, and spikes were removed (Organelli et al., 2016).

Following Organelli et al. (2017), we used the BGC-Argo measurements of $E_d(380)$ and $E_d(490)$ to compute the biological component of the diffuse attenuation coefficients for downward irradiance at 380 and 490 nm, $K_{\text{bio}}(380)$ and $K_{\text{bio}}(490)$, respectively, in the surface layer. In an analogous manner to Organelli et al. (2017), the $K_{\text{bio}}(380)$ and $K_{\text{bio}}(490)$ coefficients are here used as proxies of absorption by CDOM plus non-algal particles and phytoplankton, respectively.

For comparison, we used shipborne optical properties measured from the surface flow-through system of the vessel to estimate the diffuse attenuation coefficient, \hat{K}_d , following the model of Kirk (1991) derived from Monte Carlo modeling. Details of the methods used to measure the optical properties and model the \hat{K}_d coefficient are provided as Text S1 in Supporting Information S1. The resulting modeled $\hat{K}_d(490)$ values are analogous to the $K_{\text{bio}}(490)$ values calculated from the BGC-Argo float observations and are thus compared for each station of the SOCLIM cruise (see Section 3.3.2).

2.3.3. Regional Seasonal Cycles of BGC-Argo-Measured Bio-Optical Properties

The BGC-Argo data were sorted into distinct oceanic subregions following an approach similar to Blain et al. (2013). First, following Gray et al. (2018) for Argo floats, we applied the method of Orsi et al. (1995) to the temperature and salinity data acquired by the BGC-Argo floats (Cornec et al., 2021). This method is based on the position of the subtropical front, polar front and sea ice coverage, and results in the following zones: Subtropical Zone (STZ), SubAntarctic Zone (SAZ), Polar Front Zone (PFZ), Antarctic Southern Zone (ASZ), and Seasonal

Table 2

Number of Surface BioGeoChemical-Argo Float Measurements Used for the Computation of the Monthly Mean Cycle of the Bio-Optical Properties, for Each Subregion Considered in This Study

Subregion	January	February	March	April	May	June	July	August	September	October	November	December	Total
E_PFZ	19	18	20	25	27	28	27	19	27	25	36	26	297
E_ASZ	102	84	33	13	16	8	3	3	11	58	81	84	496
KP	36	43	20	7						17	19	17	159
W_ASZ_PFZ	53	58	32	15	17	10	16	11	20	58	60	50	400
SIZ	20	8	7	3						11	33	32	114

Ice Zone (SIZ). Second, we applied a bathymetry criterion ($<1,000$ m) to discriminate the data acquired above the KP. Finally, for the PFZ and ASZ, we considered separately the data acquired either west or east of Kerguelen (east area limited to 115°E ; east-west threshold of 70°E), being thus located either within the HNLC area or under the influence of the iron-enriched waters of the KP, respectively.

For each subregion, we used the BGC-Argo data to compute the seasonal cycle of the bio-optical properties of interest (Chla, K_{bio} , and b_{bp} coefficients) in the surface layer. For each month and each subregion, statistical parameters (mean, median and standard deviation) were calculated. Only the subregions for which a seasonal pattern of the bio-optical properties could be constructed were kept. The number of data points available for calculation of the monthly mean values is presented in Table 2. The whole procedure eventually led to the following subregions (from north to south): East PFZ (E_PFZ), East ASZ (E_ASZ), KP, West PFZ, and West ASZ are considered as one region because of the similarity in their seasonal patterns in the bio-optical properties (W_PFZ_ASZ), and SIZ.

We also determined the seasonal cycle of the bio-optical anomaly of the K_{bio} and b_{bp} coefficients. For each month and each subregion, mean monthly anomalies were computed as the differences between the BGC-Argo float-derived monthly mean values and predictions from a general empirical model, normalized to the predictions. For the K_{bio} (490) and K_{bio} (380) coefficients, the general model was that of Morel and Maritorena (2001), whilst for b_{bp} we used the global surface relationship of Barbieux et al. (2018, see their Table 3).

3. Results and Discussion

3.1. Distribution of Phytoplankton Biomass and Pigments in the SOCLIM Region

This section presents the vertical distribution of the biomass and major phytoplankton groups inferred from pigment data along the SOCLIM cruise transect (Figure 4). The surface TChla and POC levels cover a ~ 3 -fold range (Figures 4a and 4b), with the data set variability determined by station O22 located in the subtropical ocean and stations A3 (visits A3_1 and A3_2) above the KP. Station O22 is typical of stratified oligotrophic regime, with a shallow MLD (27 m), deep euphotic zone ($Z_{\text{eu}} = 111$ m), low surface biomass (TChla = 0.055 mg m^{-3} ; POC = 2.41 $\mu\text{mol L}^{-1}$), and a deep chlorophyll maximum (DCM; 0.17 mg m^{-3} at 100 m), decoupled from a shallower POC maximum (3.10 $\mu\text{mol L}^{-1}$ at 75 m). In contrast, the eutrophic stations TNS-06, TNS-08, and A3, located in the naturally iron-fertilized waters downstream of Kerguelen, are characterized by moderate to deep mixed layers (MLD = 77–180 m) and a shallow euphotic zone ($Z_{\text{eu}} = 42, 40,$ and 34 – 42 m). At these stations, the maximum biomass levels are found within the mixed layer (TChla = 1.1 – 1.7 mg m^{-3} and POC = 7.7 – 8.5 $\mu\text{mol L}^{-1}$).

The other stations exhibit intermediate biomass levels that arise from different environmental contexts. Stations O23 and O24 are under subtropical influence and show surface TChla of 0.2 mg m^{-3} , Z_{eu} of 75 m and moderate MLD (62–92 m). Further south stations O25 and O12, located in the transition zone from the subtropical to the subpolar regime, have surface TChla of 0.2 mg m^{-3} , Z_{eu} of 60 m and MLD of 93–98 m. Located in the HNLC waters upstream of Kerguelen, stations KERFIX and FS show surface TChla of ~ 0.3 mg m^{-3} and a deep MLD (173–186 m). Finally, the southernmost stations of the transect, O11 and SI, are located near the seasonal sea ice edge and show similar characteristics as found in the HNLC stations.

The results of the cluster analysis applied to the suite of biomarker pigment data reveal four phytoplankton communities that dominate the sampling region (Figure 5): (a) chlorophytes and haptophytes that are primarily

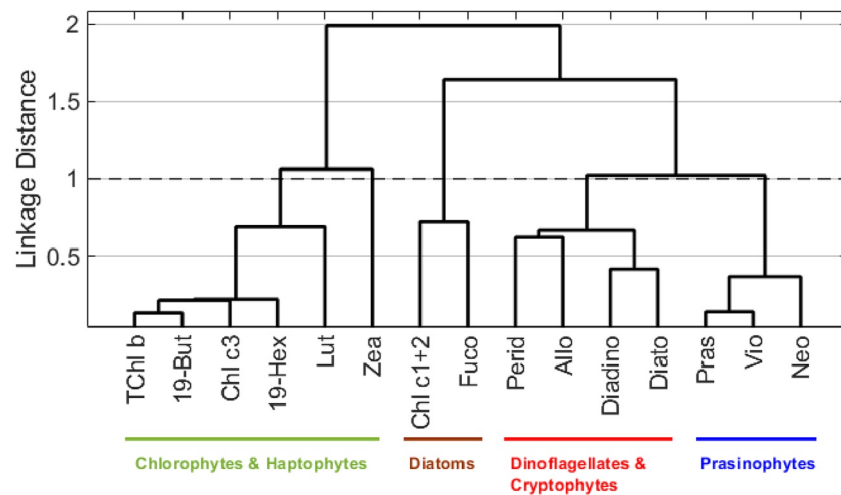


Figure 5. Dendrogram obtained from a hierarchical cluster analysis of the HPLC-determined pigment data collected at the SOCLIM sampling stations. The color code highlights four clusters of pigments indicative of four distinct phytoplankton assemblages.

characterized by the occurrence of TChlb and Hex, respectively; (b) diatoms discriminated based on their main carotenoid, Fuco, and accessory Chlc1 and Chlc2; (c) dinoflagellates and cryptophytes essentially discriminated based on Peri and Allo, respectively; and (d) prasinophytes whose main biomarker carotenoid is Pras. The distance cutoff for these four taxonomic groups is 1.0. These four clusters are quite similar to those found by Kramer and Siegel (2019) and the dominant groups reported in Claustre et al. (1997) for the SO Palmer Long-Term Ecological Research station, located west of the Antarctic Peninsula in a regime comparable to the southern open ocean (Claustre et al., 1997). In both the SOCLIM and Palmer data sets, the diatoms form a unique major cluster (linkage distance >1.5). Green algae and dinoflagellate dominate two other groups for both data sets although grouped slightly differently, with the green algae clustering with haptophytes and the dinoflagellates with the cryptophytes in SOCLIM. Prasinophytes cluster alone in the SOCLIM data set rather than with the other green algae.

In terms of spatial distribution, diatoms and dinoflagellates, which generally fall in the microplankton size class, make a dominant contribution to the phytoplankton assemblage at the stations located east of Kerguelen (TNS-06, TNS-08, and A3). This reflects in the distribution of their respective biomarker pigments, Fuco and Peri (Figures 4c and 4d), as well as their ratio to TChla (Figures 6a and 6b). These stations are characterized by maximum values of Fuco (0.40–0.78 mg m⁻³) and of the Fuco/TChla ratio (0.4–0.5). We note that TNS-06 slightly differs from its counterparts, presenting the lowest Fuco and highest Peri (0.35 mg m⁻³). Fuco also makes a substantial contribution to the pigment biomass north of Kerguelen, at stations O25 and O12, and at the southernmost stations O11 and SI.

The nanoplankton-sized community of chlorophytes and haptophytes appear to dominate the phytoplankton assemblage in the subtropical and HNLC waters to the north, west and south of Kerguelen, toward the seasonal sea ice edge. This may be seen in the distribution of Hex and TChlb (Figures 4e and 4f) and of their ratio to TChla (Figures 6c and 6d). Hex occurs in moderate to high concentrations throughout the SOCLIM transect with maximum values in the transition zone between the subtropics and the waters northeast of Kerguelen. The Hex/TChla ratio is high over the entire transect, with minimum values at the stations under the influence of the KP (TNS-06, TNS-08, and A3) where Fuco and Fuco/TChla levels are maximal. These results indicate a shift in the phytoplankton assemblage from nanoflagellate-dominated HNLC waters to diatom-dominated in iron-fertilized area, as is frequently observed in the study region (e.g., Kopczyńska et al., 1998; Lasbleiz et al., 2014; Uitz et al., 2009).

The general distribution of TChlb is similar to that of Hex from the northernmost station of the transect (O22) down to station FS (Figure 4d). Further south, the TChlb/TChla ratio decreases, with station SI having values as low as the stations near the plateau. We also note a strong (16-fold) increase in TChlb at depth at station O22 (Figure 4d). This maximum coincides with a maximum in Zea, a major carotenoid of cyanobacteria, at the DCM

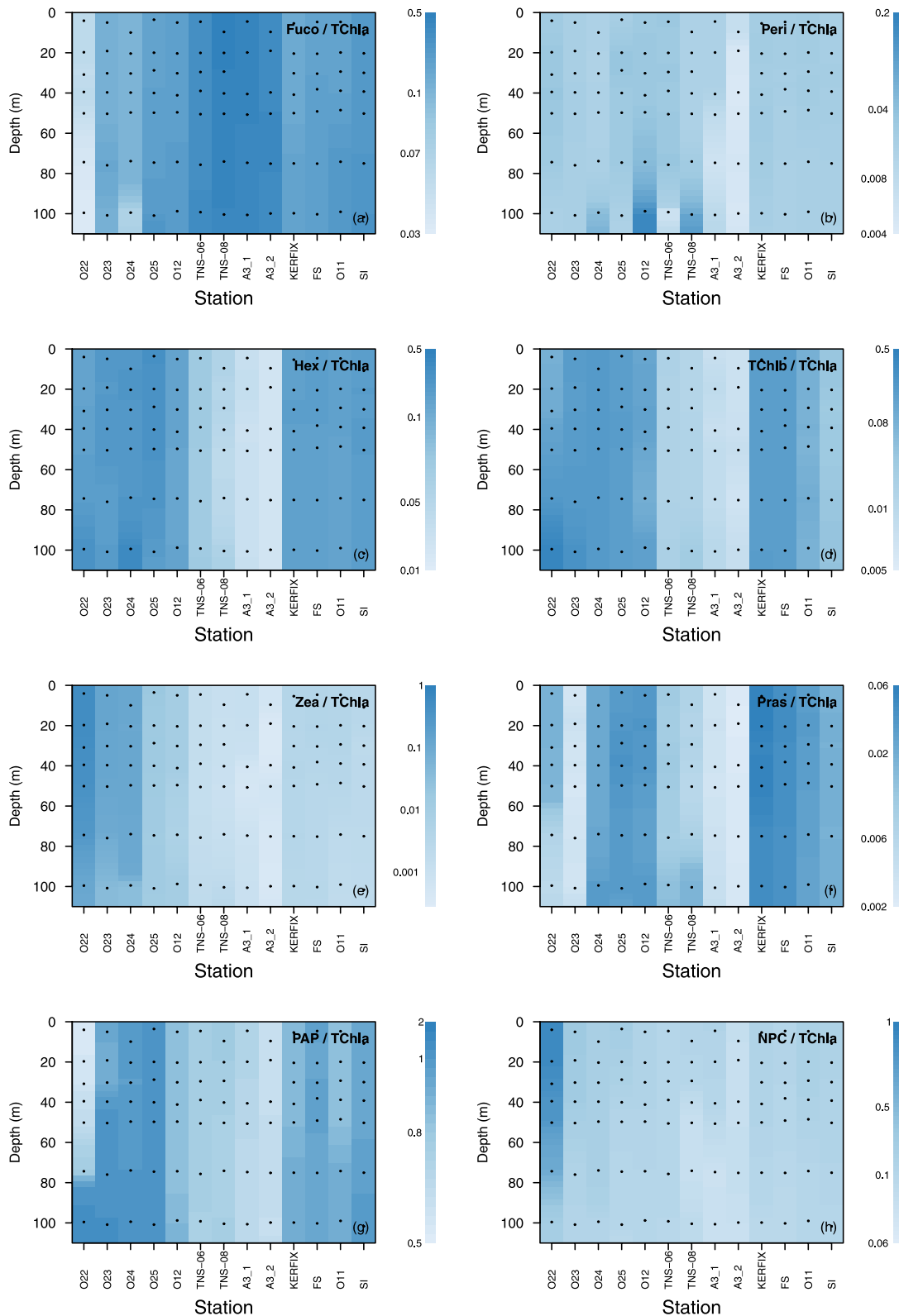


Figure 6. Vertical distribution of the ratio of the concentrations of selected pigments to total chlorophyll *a* (TChla) along the SOCLIM cruise transect: (a) fucoxanthin, Fuco; (b) peridinin, Peri; (c) 19'-hexanoyloxyfucoxanthin, Hex; (d) total chlorophyll *b*, TChlb; (e) zeaxanthin, Zea; (f) prasinolaxanthin, Pras; (g) the sum of the concentrations of photosynthetic accessory pigments, PAP; and (h) the sum of the concentrations of non-photosynthetic carotenoids, NPC.

level (Figure 4e). For all the stations south of $\sim 40^{\circ}\text{S}$, Zea shows extremely low values ($0.001\text{--}0.005\text{ mg m}^{-3}$), often below the HPLC method detection limit. In addition, the TChlb mirrors the concentration of monovinyl-chlorophyll *b*, whereas the concentration of divinyl-chlorophyll *b*, which is unique to prochlorophytes, is insignificant except at station O22 (not shown). This suggests a quasi-absence of picoprokaryotes, yet a background of chlorophytes throughout the study area, consistent with previous observations in the region (e.g., Lasbleiz et al., 2014; Uitz et al., 2009). The pigment-based results are supported by flow cytometry data from the SOCLIM cruise (Rembauville et al., 2017), which show weak and null contributions to the total cell abundance of picophytoplankton from prochlorophytes and *Synechococcus*, respectively. The distribution of Pras (Figures 4h and 6f) suggests that the fourth cluster of prasinophytes occurs, similarly to chlorophytes, at the north, west and south of Kerguelen, albeit in much lower abundance. Their maximum contribution to the phytoplankton biomass occurs at the HNLC KERFIX and FS stations.

In addition to the distribution of these main phytoplankton taxa groups, the vertical distribution of the pigment ratios contains information on the physiological status of the communities (Figure 6). Indeed, the pigment composition of phytoplankton not only varies with phytoplankton taxa but also with environmental conditions, particularly light. Phytoplankton cells have the ability to adjust their pigment pool in order to optimize light harvesting (PAP) and protect from damages caused by excess light energy (NPC). Hence the vertical distribution of PAP and NPC concentrations relative to phytoplankton biomass (or TChla) varies within the water column as a result of light conditions and history (within timescales of a few hours to days). In typical stable (stratified) conditions one would observe an increase in the ratios NPC/TChla in the surface and PPC/TChla at depth (Brunet et al., 2011). Over the SOCLIM transect, the PAP/TChla ratio (Figure 6g) shows low values at the stations TNS-06, TNS-08, and A3, dominated by diatoms, as well as O12 which likely hosts dinoflagellates (Figures 4c and 4d). The NPC/TChla ratio shows relatively low levels along the entire transect, except at O22 due to elevated Zea/TChla values under high light conditions (Figures 6e and 6h). We also note that, apart from the subtropical station O22 that is characterized by the presence of a DCM, the pigment ratios show a relatively homogeneous vertical distribution at all the sampling stations. This indicates that the phytoplankton populations are demonstrating depth-independent photoacclimation. The SOCLIM stations exhibit large variations in the MLD and stratification status as indicated by the position of the MLD with respect to that of the Z_{eu} (Figure 4a). Whereas, for example, station A3 has a MLD and Z_{eu} of 150 and 35 m, respectively, O12 has much more similar values of MLD and Z_{eu} (75 vs. 65 m, respectively). Thus, despite variations in MLD, this suggests (ongoing or recent) vertical mixing that takes over photoacclimation processes. Further, this also indicates that surface phytoplankton communities detected by remote sensing will exhibit optical proxy values closer to deeper light-limited populations, reflecting mean levels found in the mixed layer.

3.2. Bio-Optical Relationships From Shipborne Measurements

3.2.1. Phytoplankton Absorption Coefficient

During the SOCLIM cruise, the spectral phytoplankton absorption coefficients at 676 nm, $a_{\text{ph}}(676)$, and 440 nm, $a_{\text{ph}}(440)$ vary by a factor of ~ 10 (Figures 7a and 7b). The minimum and maximum values were found at stations O24 and A3_1, respectively. As typically observed in the open ocean (Bricaud et al., 1995, 2004), both the $a_{\text{ph}}(440)$ and $a_{\text{ph}}(676)$ coefficients covary positively with TChla following a power function (Table 3).

In the surface waters ($<10\text{ m}$ depth), the $a_{\text{ph}}(676)$ -to-TChla relationship is very similar to that of Bricaud et al. (1995, 2004), which was developed using a data set combining measurements from temperate, equatorial and subtropical open oceans (Figure 7a). In contrast, the SOCLIM $a_{\text{ph}}(440)$ -to-TChla relationship deviates significantly from Bricaud's general relationships (Figure 7b). In fact, the SOCLIM $a_{\text{ph}}(440)$ values are more than a factor of 2 lower than that predicted by Bricaud et al. (2004) for a given chlorophyll concentration, and the trend becomes more pronounced as TChla increases. Whilst the measurements taken in the iron-enriched waters downstream of Kerguelen substantially depart from the general model, those from subtropical waters (stations O22 and O23) are close to the regression model of Bricaud et al. (2010) based on data from the South Pacific Subtropical Ocean. The proxy most sensitive to photoacclimation, $a_{\text{ph}}(440)$, and the communities most impacted by deep mixing reveal the largest deviation from global values, while the proxy least sensitive to photoacclimation, $a_{\text{ph}}(676)$, and the communities least impacted by deep mixing are in line with global values.

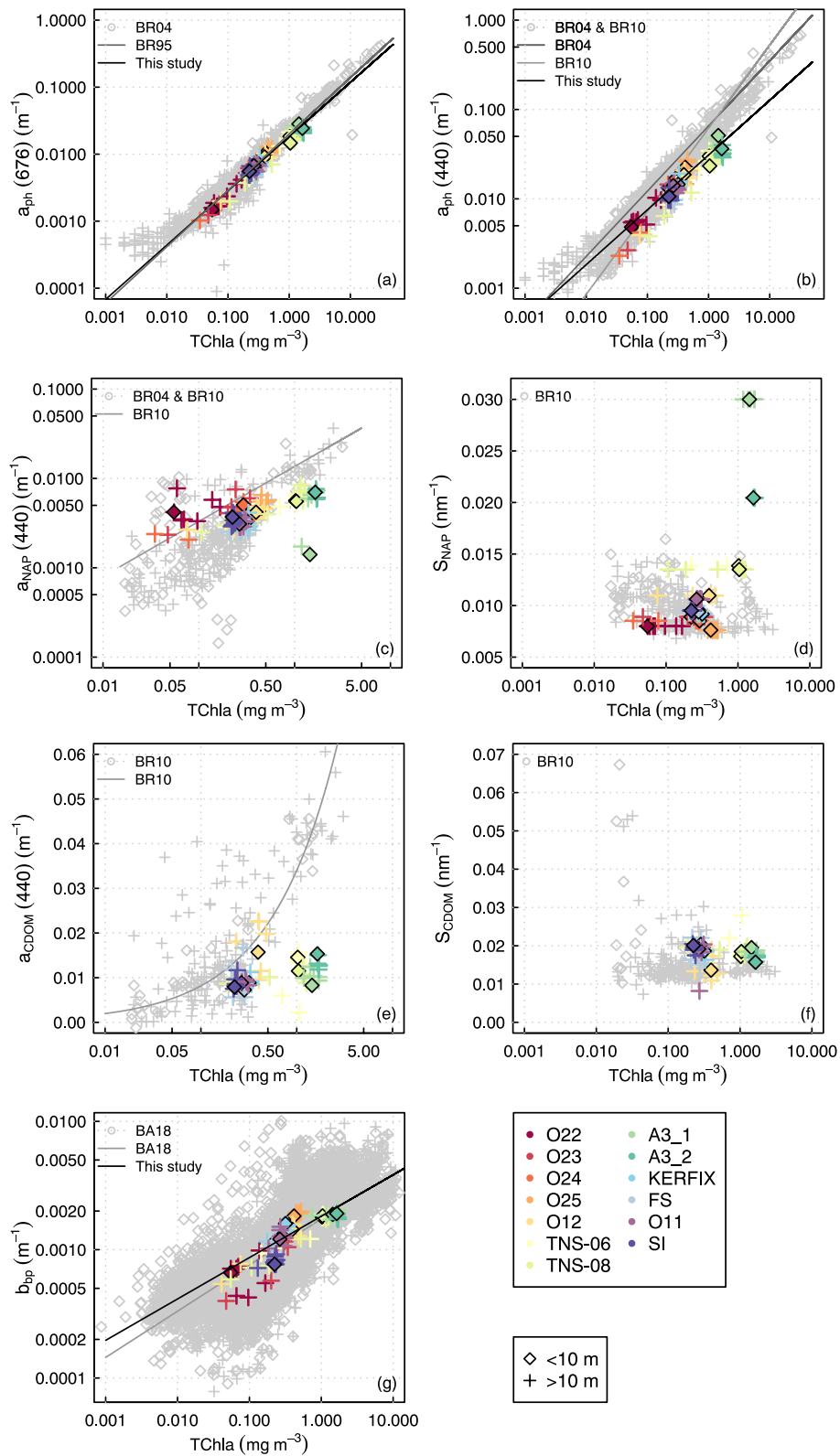


Figure 7.

Table 3
Bio-Optical Relationships Computed for the Surface SOCLIM Data Set

Relationship	r^2	p
$a_{\text{ph}}(440) = 0.031 \text{ TChla}^{0.613}$	0.93	***
$a_{\text{ph}}(676) = 0.018 \text{ TChla}^{0.810}$	0.98	***
$b_{\text{bp}}(700) = 0.002 \text{ TChla}^{0.322}$	0.77	***

Note. Significance level of the regression model (*** $p < 0.001$).

For the surface waters, we quantify the deviation in the $a_{\text{ph}}(440)$ -to-TChla relationship using an anomaly index, defined as the difference between the measured $a_{\text{ph}}(440)$ values and the predictions from the Bricaud et al. (2004) general relationship using as input the HPLC-determined TChla, normalized to the predictions. The computed anomaly index varies between -35% and -65% in the surface layer, with minimal values found in oligotrophic conditions (station O25) and maximal values downstream of Kerguelen (station TNS-08). This anomaly index reflects, and positively covaries with, a flattening of the phytoplankton absorption spectra, as indicated by the $a_{\text{ph}}(440)/a_{\text{ph}}(676)$ ratio (Pearson correlation coefficient $r = -0.81$, $p = 0.002$). This flattening can be seen on the chlorophyll-specific phytoplankton spectra presented in Figure S1 in Supporting Information S1.

Atypical phytoplankton absorption spectra characterized by a flattened shape with low values of $a_{\text{ph}}(440)$ relative to $a_{\text{ph}}(676)$ are frequent in the SO, as reported in previous studies considering low- versus high-latitude environments (Mitchell & Holm-Hansen, 1991b; Reynolds et al., 2015; Sosik et al., 1992). Theory and observations demonstrate that this feature generally results from a pigment packaging effect occurring in phytoplankton cells, which is a function of increased phytoplankton cell size and/or the intracellular pigment content in response to photoacclimation (Bricaud et al., 1981; Duyens, 1956; Robinson et al., 2021; Sathyendranath et al., 1987). A decreased contribution of accessory pigments absorbing light in the blue is often observed when the contribution of picoprokaryotes to the phytoplankton assemblage is reduced, and thus may contribute to the observed pattern (Bricaud et al., 2004; Uitz et al., 2008). In the next section, we investigate the role of these factors on the observed anomaly in the surface SOCLIM cruise data set.

3.2.2. Sources of Anomalies in the $a_{\text{ph}}(440)$ -To-Chl Relationship

In order to investigate the anomaly in the surface SOCLIM $a_{\text{ph}}(\lambda)$ spectra, we discuss the correlation of the $a_{\text{ph}}(440)/a_{\text{ph}}(676)$ ratio, used as an index of the flattening of $a_{\text{ph}}(\lambda)$, with various biological variables (Figure 8 and Table 4). First, we consider the community weighted index ESD_{CW} , which is an independent indicator of the mean size of the phytoplankton community, long known to be a major determinant of the package effect. In order to account for the influence of the intracellular TChla driven by size-dependent photoacclimation in phytoplankton cells, we consider the $\text{TChla}/N_{\text{tot}}$ ratio (with N_{tot} the total cellular abundance determined from flow cytometry and microscopy analyses). In addition, we used several indicators of the pigment composition, which results from the phytoplankton taxonomic assemblage and is anticipated to affect the shape of the $a_{\text{ph}}(\lambda)$ spectra: the ratios to TChla of Fuco, Peri, Hex, TChlb, Zea, and Pras. Finally, we considered the TAP, PAP, and NPC to TChla ratios, which yield the relative contribution of total accessory pigments, photosynthetic pigments and photoprotective carotenoids to the phytoplankton biomass, respectively, and result from the combined effects of taxonomy and photoacclimation.

The analysis shows that the $a_{\text{ph}}(440)/a_{\text{ph}}(676)$ ratio correlates linearly with the phytoplankton size proxy ESD_{CW} ($r^2 = 0.9$, $p < 0.001$; Figure 8a and Table 4) and with the ratio of TAP/TChla ($r^2 = 0.75$, $p < 0.001$; Figure 8c). It is also highly correlated in a lognormal manner with the indicators of photoacclimation $\text{TChla}/N_{\text{tot}}$ ($r^2 = 0.89$, $p < 0.001$; Figure 8b) and NPC/TChla ($r^2 = 0.91$, $p < 0.001$; Figure 8d). These relationships are largely explained by ratios of accessory pigments to TChla. In particular the absorption ratio is negatively and linearly correlated with Fuco/TChla ($r^2 = 0.73$, $p < 0.001$; Figure 8e) and positively correlated in a lognormal manner to the other accessory pigment (Peri, Hex, TChlb, Zea, and Pras) ratios to TChla (see Figure S2 in Supporting Information S1).

Therefore, the degree of flattening of the $a_{\text{ph}}(\lambda)$ spectrum, which largely explains the anomaly in the $a_{\text{ph}}(440)$ -to-TChla relationship, appears to be controlled by two main factors, the composition of phytoplankton

Figure 7. Scatterplot of selected measured optical properties as a function of total chlorophyll a concentration (TChla): (a) phytoplankton absorption coefficients at 676 nm, $a_{\text{ph}}(676)$ and (b) 440 nm, $a_{\text{ph}}(440)$; (c) non-algal particle absorption coefficient at 440 nm, $a_{\text{NAP}}(440)$; (d) slope of the non-algal particle absorption spectrum, S_{NAP} ; (e) colored dissolved organic matter (CDOM) absorption coefficient at 440 nm, $a_{\text{CDOM}}(440)$; (f) slope of the CDOM absorption spectrum, S_{CDOM} ; (g) the particulate backscattering coefficient at 700 nm, $b_{\text{bp}}(700)$. The color code indicates the SOCLIM cruise sampling stations and the symbols the depth of acquisition. Values within the layer 0–150 m are shown, with surface data represented by the diamond symbols. The bio-optical relationships for the surface layer in this study are shown as the black line. We also show in gray color previously published measurements and derived bio-optical relationships from various open ocean regions: Subequatorial Pacific, Atlantic and Mediterranean from Bricaud et al., 2004 (BR04), Southeast Pacific from Bricaud et al. (2010) (BR10), and global ocean from Barbieux et al. (2018) (BA18). Spectra from which these observations are derived are presented in Figures S1 and S3 in Supporting Information S1.

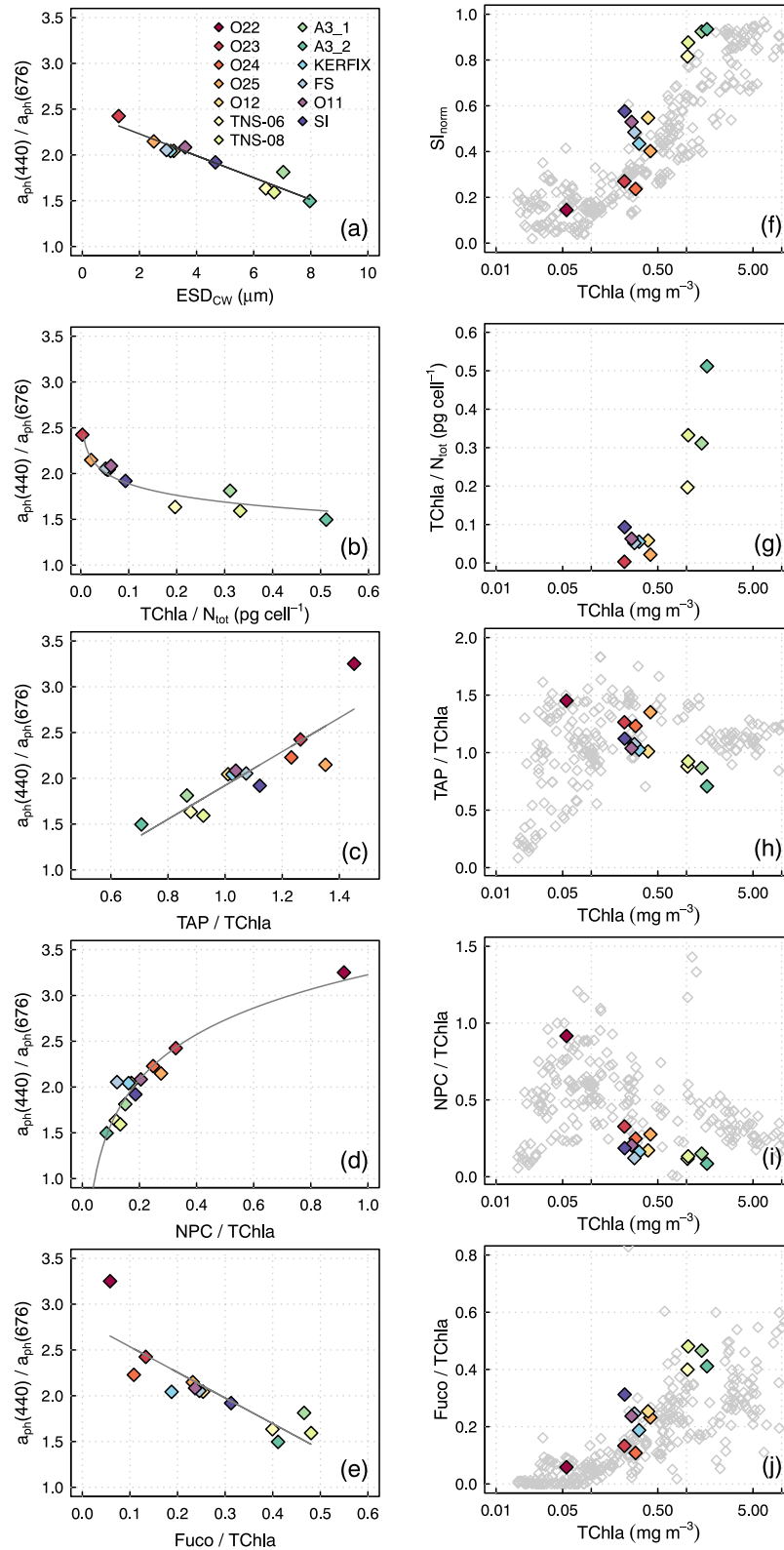


Figure 8.

Table 4
Correlation Coefficients Between the $a_{ph}(440)/a_{ph}(676)$ Ratio, Used as an Indicator of the Flattening of the Phytoplankton Absorption Spectrum, $a_{ph}(\lambda)$, and Selected Biological Variables Calculated for the SOCLIM Data Set

Variable	Regression type	r^2	Significance
ESD _{CW}	Linear	0.91	***
TChla/ N_{tot}	Lognormal	0.89	***
TAP/Chl	Linear	0.75	***
NPC/Chl	Lognormal	0.91	***
Fuco/TChla	Linear	0.73	***
Peri/TChla	Linear	0.11	*
Hex/TChla	Linear	0.27	*
TChlb/TChla	Lognormal	0.34	*
Zea/TChla	Lognormal	0.84	***
Pras/TChla	Lognormal	0.19	ns

Note. We also indicate the type of regression model (linear or lognormal) fitted to the data and the significance level of the regression (* $p < 0.05$; ** $p < 0.01$; *** $p < 0.001$; ns: not significant).

communities and their photoacclimation to low-light conditions. Regarding the first, an increase in the average size of the phytoplankton community coincides with maximum flattening concomitant with maximum cell size and relative contribution of diatoms, as determined from the Fuco/TChla ratio. Indeed, except for the northernmost stations of the SOCLIM transect (O22–O25), the data set displays higher values of the SI_{norm} index (Figure 8f) and Fuco/TChla (Figure 8j) than non-polar regions with similar TChla (Bricaud et al., 1995, 2004). This suggests that the SOCLIM subpolar waters are dominated by a phytoplankton assemblage comprising a much larger proportion of relatively large cells, especially diatoms, than other non-polar regions. The hypothesis of the dominance of a limited number of phytoplankton groups in the SOCLIM subpolar waters compared to non-polar regions is supported by lower-than-expected values of the ratios to TChla of the main biomarker pigments apart from Fuco (Figure 8j), including at stations where the phytoplankton assemblage is not dominated by diatoms (i.e., Peri, Hex, TChlb, and Zea; Figure S2 in Supporting Information S1).

Second, the degree in $a_{ph}(\lambda)$ flattening and the $a_{ph}(440)$ -to-TChla anomaly is also influenced by the intracellular TChla content (Figure 8b), resulting from both photoacclimation and phytoplankton composition. The $a_{ph}(\lambda)$ flattening appears to respond positively to a low contribution of TAP and NPC to TChla, the phytoplankton communities being essentially acclimated to low light conditions, except for the subtropical area, as suggested by the uniform

vertical distribution of the pigments to TChla ratios (Figure 6). Additionally, the SOCLIM data set shows an unusual TAP-to-TChla relationship, with the TAP/TChla ratio decreasing with TChla, and much lower TAP/TChla and NPC/TChla values compared to data from non-polar regions (Figures 8h and 8i). This trend is especially pronounced for the stations under the influence of the KP (TNS-06, TNS-08, and A3).

These results indicate that the absorption anomaly in the blue waveband is driven by (a) the transition between communities dominated by large diatoms at one extreme, and all other nanoplankton communities at the other extreme, and (b) the photoacclimation of the phytoplankton to the low light levels they experience due to deep mixing. Overall, these results are consistent with several previous studies conducted in the SO, highlighting phytoplankton size (Ferreira et al., 2017; Robinson et al., 2021), and more generally phytoplankton community composition (Brody et al., 1992; Ferreira et al., 2013), as a major determinant of the absorption anomaly due to their influence on size and pigment composition. A few studies privileged the role of acclimation to chronic low light due to deep mixing, large solar zenith angle and frequent cloud cover (Mitchell, 1992; Mitchell & Holm-Hansen, 1991b; Sosik et al., 1992), which we interpret for the SOCLIM region as a major, yet not unique, driver. The contribution of these analyses is highlighted in combining how taxonomic composition, taxon-specific optical properties, photoacclimation and hydrographic MLD explain the bio-optical anomaly.

3.2.3. Non-Algal Particle Absorption Coefficient

The values of non-algal particle absorption coefficient at 440 nm, $a_{NAP}(440)$ show little variability along the SOCLIM transect (0.001–0.006 m^{-1} at surface; Figure 7c) and, while the values fall within the range of measurements in various open ocean waters (Bricaud et al., 2004), they are a factor of 5 lower than expected based upon the global relationship of Bricaud et al. (2010), except for the northernmost stations of the transect, O22 in particular. In keeping with our observations of the phytoplankton absorption coefficient, $a_{ph}(440)$, this trend is more pronounced as TChla increases. A simple light absorption budget, presented as a ternary diagram in

Figure 8. Scatterplots of the distribution of (left column) the $a_{ph}(440)/a_{ph}(676)$ ratio as a function of selected variables, and (right column) selected variables a function of the total chlorophyll *a* concentration (TChla). Specifically, the selected variables are: phytoplankton size represented by (a) the mean community weighted equivalent spherical diameter ESD_{CW} and (f) the normalized pigment-based size index (SI_{norm}); (b, g) the TChla normalized to the total cellular abundance, TChla/ N_{tot} ; (c, h) the ratio of the concentrations of total accessory pigments (TAP) to TChla, TAP/TChla; (d, i) the ratio of the concentrations of non-photosynthetic carotenoids (NPC) to TChla, NPC/TChla; (e, j) the ratio of the concentrations of fucoxanthin to TChla, Fuco/TChla. The color code indicates the SOCLIM cruise sampling stations, the diamond symbol indicates surface samples. Lines indicate best linear or lognormal fits. When available, we show in gray color previously published measurements from the Subequatorial Pacific Ocean, Atlantic Ocean and Mediterranean Sea (Bricaud et al., 2004) and from the Southeast Pacific Ocean (Bricaud et al., 2010). The $a_{NAP}(440)$ and S_{NAP} estimates for station A3 are shown for information purposes but are not considered in the analysis (see Section 2.2.3).

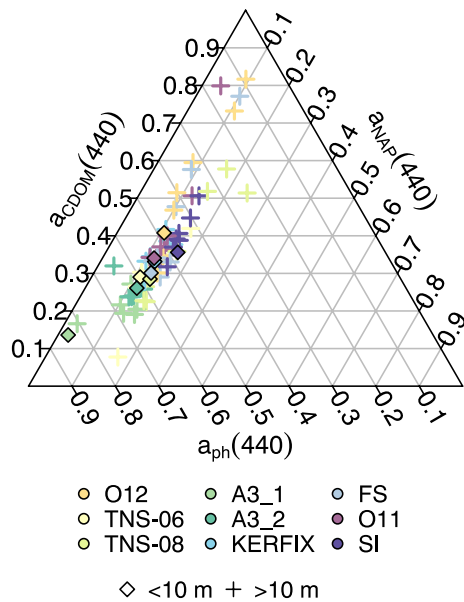


Figure 9. Ternary diagram showing the relative contribution to the absorption coefficient at 440 nm of phytoplankton, $a_{ph}(440)$, non-algal particles, $a_{NAP}(440)$, and colored dissolved organic matter, $a_{CDOM}(440)$. The color code indicates the SOCLIM cruise sampling stations and the symbols the depth of acquisition. Values within the layer 0–150 m are shown, with surface data represented by the diamond symbols. The a_{NAP} estimates for station A3 are shown for information purposes but are not considered in the analysis (see Section 2.2.3).

Figure 9, indicates a weak contribution (2%–17% in the surface layer) of non-algal particles to the absorption coefficient at 440 nm, regardless of the station.

Low $a_{NAP}(440)$ values are consistent with a large body of literature reporting contribution by non-algal particulate matter to absorption in high latitudes compared to temperate waters (Clementson et al., 2001; Figueroa, 2002; Hirawake et al., 2000; Mitchell & Holm-Hansen, 1991b; Sosik et al., 1992). Yet a recent study by Robinson et al. (2021), based on a circumpolar navigation, indicates that NAP makes a dominant contribution to the particulate absorption budget in a large range of subpolar conditions, a feature we do not observe in the SOCLIM data set. A possible explanation for this difference is that SOCLIM happened earlier in the year, in spring during the onset of phytoplankton blooms when particulate matter is low, as corroborated by the low ratios of phaeopigments to TChla that are suggestive of weak grazing activity (not shown). In contrast, the study of Robinson et al. (2021) is based on data acquired in summer, as most studies conducted in the SO, when peak bloom or post bloom conditions associated with grazing and particulate matter cycling result in higher overall particulate matter.

The slope of $a_{NAP}(\lambda)$, S_{NAP} , does not show any significant intrinsic relationship with TChla (Figure 7d), but varies within a relatively large range (from 0.007 to 0.014 nm^{-1} , excluding the observations from the shallow A3 stations with high concentrations of suspended lithogenic sediments), similar to previous observations in the South Pacific Ocean (Bricaud et al., 2010). Minimum values are found at stations from the subtropical area (O22–O24) and maximum values at the stations located in the naturally fertilized area (TNS-06 and TNS-08). Although the contribution of non-algal particles to absorption appears weak and relatively constant over the entire study region,

the observed variability in S_{NAP} suggests a variable contribution of biogenic, detrital and mineral particles to the NAP pool depending on the station, yet independent of TChla.

3.2.4. Absorption Coefficient of Color Dissolved Organic Matter

The absorption coefficient of CDOM at 440 nm, $a_{CDOM}(440)$, was determined at 9 out of the 12 sampling stations (no data available north of 47°S) as shown in Figure 7e. The full $a_{CDOM}(\lambda)$ spectra, provided as Supporting Information S1 (Figure S3), show a classic featureless exponential shape, indicative of an absence of absorbing pigments (e.g., phaeopigments, micro-sporine like amino acids, cytochromes) freely-dispersed in water. Similar to $a_{NAP}(440)$, the measured $a_{CDOM}(440)$ values (0.007–0.016 m^{-1} at surface) exhibit no extrinsic dependence on TChla. The $a_{CDOM}(440)$ values are comparable to, or 30%–50% lower than those measured in the South Pacific Subtropical Ocean by Bricaud et al. (2010) for TChla < 0.5 mg m^{-3} . For the stations TNS-06, TNS-08, and A3, located downstream of Kerguelen, the $a_{CDOM}(440)$ values are significantly lower than expected from the Bricaud et al. (2010) relationship (Figure 7e). In spite of relatively low $a_{CDOM}(440)$ values, the contribution of CDOM to absorption at 440 nm varies within a non-negligible range. It reaches 41% in the surface layer of the northernmost station (O12) for which $a_{CDOM}(440)$ was measured, coinciding with a minimum contribution from phytoplankton (48%; Figure 9). Conversely, the contribution of CDOM to absorption is reduced at stations where phytoplankton absorption dominates (e.g., 28% and 60% for $a_{CDOM}(440)$ and $a_{ph}(440)$, respectively, in the surface layer of TNS-08; Figure 9). The $a_{CDOM}(440)$ measurements made during SOCLIM stand at the lower end of the range of data from different regions of the SO such as the Antarctic PFZ (Reynolds et al., 2001), South of Australia (Clementson et al., 2001), the Ross Sea (D'Sa et al., 2021; Reynolds et al., 2001), South Georgia Island (Del Castillo & Miller, 2011), or the Antarctic Peninsula (Ferreira et al., 2018). In contrast, the values of the $a_{CDOM}(\lambda)$ slope, S_{CDOM} (Figure 7f), vary within the range 0.01–0.02 nm^{-1} (for surface waters), consistently with values previously reported for non-polar (Bricaud et al., 2010) as well as polar waters (Ferreira et al., 2018; Reynolds et al., 2001).

The present results are consistent with the view that CDOM has overall a moderate optical fingerprint in the SO compared to high-latitude waters of the northern hemisphere (Nelson & Siegel, 2013; Reynolds et al., 2015). The

magnitude of CDOM absorption in the blue is comparable to the average value for phytoplankton and a factor of 2 larger than that of NAP. And while the proportions of the components change over the sampling region, they are largely driven by variations in phytoplankton rather than variations in CDOM. While the presence of CDOM in coastal environments may be explained by terrestrial inputs in oceanic regions under the influence of river or ice melt run-offs (e.g., Andrew et al., 2013; Bricaud et al., 1981; Matsuoka et al., 2012), CDOM accumulation in the open ocean typically results from biological (microbial and phytoplankton) activity. However, the timescales of biological activity and CDOM production are decoupled, leading to generally poor $a_{\text{CDOM}}(\lambda)$ -to-TChla relationship (Bricaud et al., 1981; Reynolds et al., 2001). In stratified oligotrophic conditions, CDOM production is largely affected by picophytoplankton (Bricaud et al., 2010; Organelli & Claustre, 2019), a phytoplankton group rarely observed in southern waters. Reynolds et al. (2001) report high $a_{\text{CDOM}}(\lambda)$ values associated with *Phaeocystis* blooms in the Ross Sea and low values for diatoms-dominated waters, which appears consistent with the SOCLIM data showing a limited contribution of CDOM at the diatom-dominated bloom stations. Similar to the low $a_{\text{NAP}}(\lambda)$ values, the low $a_{\text{CDOM}}(\lambda)$ values in the present data set could also arise from the seasonal context. The SOCLIM cruise sampled early bloom conditions that may be associated with low $a_{\text{CDOM}}(\lambda)$ coefficients, whereas $a_{\text{CDOM}}(\lambda)$ tends to increase as blooms develop (Organelli et al., 2014). Finally, photooxidation in highly stratified surface waters reduces $a_{\text{CDOM}}(\lambda)$, yielding strong declines with depth (e.g., Bricaud et al., 1981; Nelson et al., 1998), a feature that is not observed for SOCLIM, and is consistent with mixing rates exceeding photooxidation rates.

3.2.5. Particulate Backscattering Coefficient

The SOCLIM cruise data set covers a broad range of values of the particulate backscattering coefficient at 700 nm, $b_{\text{pp}}(700)$, as shown in Figure 7g (0.0007–0.0019 m^{-1} for surface data). In addition, these data fall within the average range of values observed in the global ocean, and display the extrinsic dependence on TChla, in agreement with the relationship established for the surface ocean based on a global BGC-Argo database (Barbieux et al., 2018). These results overall suggest an absence of $b_{\text{pp}}(700)$ anomaly, compared to the global ocean, in the SOCLIM data set.

The robust $b_{\text{pp}}(700)$ -to-TChla relationship with reduced scattering in the data, as observed in Figure 7g, indicates a strong coupling between $b_{\text{pp}}(700)$ and the phytoplankton biomass, supporting the covariation of biogenic particles in the study region. To second order, photoacclimation may affect the b_{pp} -to-TChla relationship, leading to an increase in the intracellular TChla of algae independently of carbon biomass under low irradiance. This feature is observed in the subtropical waters sampled at stations O22 and O23, where $b_{\text{pp}}(700)$ is lower than predicted based on TChla at depth (Figure 7g).

3.3. Seasonal Cycles of Bio-Optical Properties Measured by BGC-Argo Floats

3.3.1. Phytoplankton Chlorophyll Biomass

The monthly mean cycle of the Chla concentration derived from the BGC-Argo float measurements, corrected using either a slope factor value of 2 (Chla_F2) or 4 (Chla_F4), is shown for each subregion in Figure 10. Except for the KP (Figure 10c), all the subregions exhibit a monthly mean Chla cycle characterized by a single maximum associated with the summer phytoplankton bloom, in December for the E_PFZ (Figure 10a), E_ASZ (Figure 10b) and W_ASEZ_PFZ (Figure 10d), and in March for the SIZ (Figure 10e). This time lag may be explained by a latitudinal difference, with phytoplankton in the SIZ benefiting from favorable light conditions later in the season as ice retreats (Thomalla et al., 2011; Uchida et al., 2019). The seasonal bloom is associated with large Chla values in the E_ASZ (maximum of the mean cycle within 0.75–1.5 mg m^{-3}) and SIZ (0.9–1.8 mg m^{-3}), and moderate values in the HNLC waters of the W_ASZ_PFZ (0.5–1 mg m^{-3}) and E_PFZ (0.3–0.6 mg m^{-3}). In the KP zone, the monthly mean Chla cycle shows two peaks, in November and January, associated with two blooms in spring and summer, as has been previously observed in the area (Blain et al., 2021).

For comparison purposes, the HPLC-determined TChla data acquired at the SOCLIM stations are overlaid onto the mean seasonal cycle of the corresponding subregions, with stations TNS-06 and TNS-08 located in the E_ASZ (Figure 10b), KERFIX and FS in the W_ASZ_PFZ (Figure 10d), SI in the SIZ (Figure 10e), and A3_1 and A3_2 in the KP zone (Figure 10c). We find reasonable agreement between the monthly mean float-based and shipborne HPLC-determined TChla during the SOCLIM cruise. While the cruise was carried out at the beginning of the blooms, the floats captured the blooms entirely.

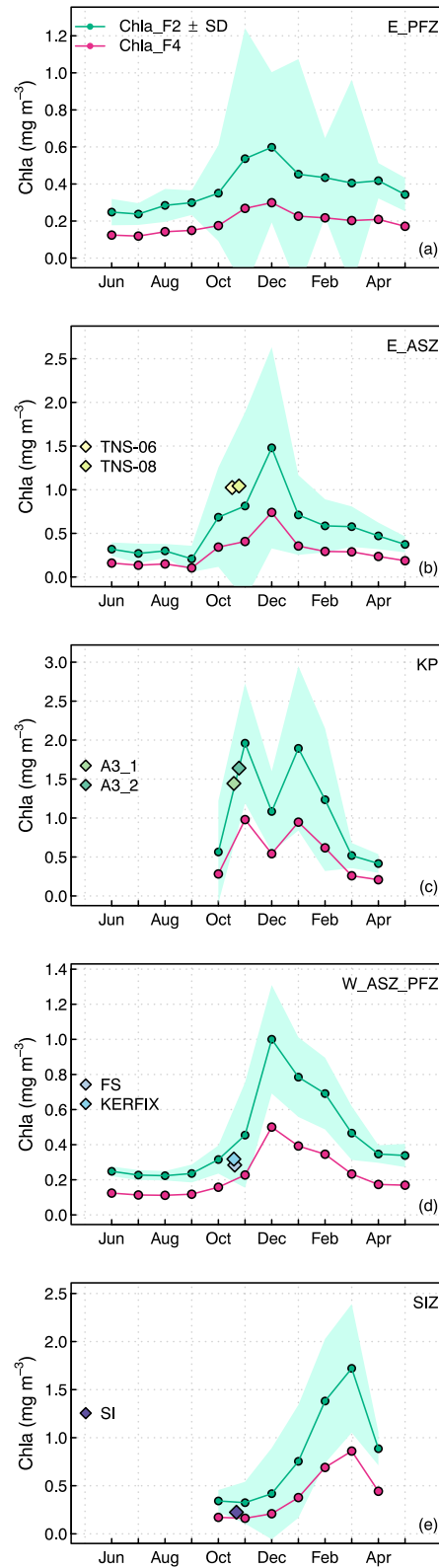


Figure 10.

3.3.2. Seasonal Variation in the Biological Component of the Diffuse Attenuation Coefficient

As in Organelli et al. (2017), we use the $K_{\text{bio}}(490)$ coefficient derived from the BGC-Argo float radiometric measurements as a proxy for the phytoplankton absorption coefficient. The float measurements are compared to predictions from the general bio-optical model of Morel and Maritorena (2001) using as input either Chla_F2 or Chla_F4 (Figures 11a–11e). In an analogous manner to that used for $a_{\text{ph}}(440)$, we computed an anomaly index for $K_{\text{bio}}(490)$ (in %) as the difference between the float-derived monthly mean value and the prediction from the Morel and Maritorena (2001) model, normalized to the predictions (Figures 11f–11j). The $\hat{K}_a(490)$ values estimated from the Kirk (1991) model provided independent validation of both the measured and modeled $K_{\text{bio}}(490)$ values for the regions sampled during the SOCLIM cruise.

The monthly mean $K_{\text{bio}}(490)$ values generally follow the seasonal cycle of Chla (Figures 11a–11e), indicative of a strong correlation between absorption by phytoplankton and, possibly, other covarying optically active constituents, and chlorophyll biomass in all considered subregions. For most regions, during a time period starting from the apex of the bloom (November or December depending on the region) until the end of summer (March or April), the measured $K_{\text{bio}}(490)$ values tend to decrease (Figures 11a–11e). This period coincides with a decrease of the anomaly index that often becomes negative, which indicates that the $K_{\text{bio}}(490)$ measurements are lower than the model predictions (Figures 11f–11i). In the lower biomass regimes encountered in the fall, winter and spring, the pattern is more complex. The $K_{\text{bio}}(490)$ measurements are lower than, or comparable to predictions when Chla_F2 is used as input to the model, and comparable to, or even higher than the predictions based on Chla_F4 for some of the regions, that is, KP and, to a lesser extent, E_ASZ and E_PFZ (Figures 11a–11c). We also note regional variability in the amplitude of the seasonal cycle of the $K_{\text{bio}}(490)$ anomaly, which is reduced (i.e., a “flatter” seasonal cycle) in the E_PFZ, W_ASZ_PFZ, and SIZ zones (~35%), and more pronounced in the zones under the influence of Kerguelen, that is, E_ASZ (48%) and KP (65%).

The low to negative $K_{\text{bio}}(490)$ anomaly observed in our results during the bloom season indicate lower-than-expected phytoplankton absorption in the blue spectral domain for the considered Chla levels, consistent with previous observations in the SO (e.g., Dierssen & Smith, 2000; Ferreira et al., 2017; Robinson et al., 2021; Sosik et al., 1992). This could be due to an increase in the average size of the phytoplankton assemblage during the bloom season and/or an increase in the intracellular Chla content resulting from photoacclimation to low light conditions. Both factors are corroborated by the seasonal cycle of the measured $K_{\text{bio}}(490)$ /Chla ratio (Figures 12a–12e), showing a decrease during the apex of the bloom accompanied with a simultaneous decrease in the measured $b_{\text{bp}}(700)$ /Chla ratio which can be used as a crude proxy for the POC/Chla ratio (Figures 12f–12j). The seasonal cycle of the average PAR in the mixed layer, PAR_{ML} , appears to covary with Chla in the lower biomass regimes (E_PFZ and W_ASZ_PFZ), but shows moderate to low values at the Chla peak in the higher biomass regimes (E_ASZ, KP, and SIZ; Figures 12k–12n). Thus, photoacclimation could, at least partly, explain the negative $K_{\text{bio}}(490)$ anomaly in the latter, probably due to self-shading of phytoplankton cells (Blain et al., 2013).

In contrast, the moderate to low values of the $K_{\text{bio}}(490)$ anomaly generally found during the low biomass season may be attributed to the presence of small phytoplankton cells, a result consistent with high values of the (measured) $K_{\text{bio}}(490)$ /Chla ratio. Relatively high values of the (measured) $b_{\text{bp}}(700)$ /Chla ratio in winter and early spring, concomitant with relatively low PAR_{ML} levels, suggest that the small phytoplankton population is not light-limited or that the effect of light limitation (decrease in absorption coefficient per Chla unit) is compensated by that of small cell size (increase per Chla unit). The SO is expected to be light-limited and dominated by small cells in the winter months. Our results confirm this hypothesis, yet suggest that the phytoplankton absorption properties do not appear to be strongly affected by photoacclimation during this season, due to an opposite effect of cell size.

We note that, for the KP zone (Figure 10c), the second Chla peak is accompanied by a second peak in $b_{\text{bp}}(700)$, but not by a $K_{\text{bio}}(490)$ maximum as is the first (Figure 11c). This suggests that the second phytoplankton biomass increase in January is associated with a change in the composition and/or physiology of the phytoplankton population compared to that in November. The seasonal cycle of the $K_{\text{bio}}(490)$ /Chla and $b_{\text{bp}}(700)$ /Chla ratios show local

Figure 10. Monthly mean of the chlorophyll *a* concentration derived from the BGC-Argo float fluorescence measurements (Chla, mg m^{-3}) for the 5 regions considered in this study: (a) the East Polar Front Zone, E_PFZ; (b) the East Antarctic Southern Zone, E_ASZ; (c) the Kerguelen Plateau, KP; (d) the West Polar Front Zone and West Antarctic Southern Zone, W_PFZ_ASZ; (e) the Seasonal Ice Zone, SIZ. The green and pink curves represent the Chla values obtained using the global factor of 2 (Chla_F2) or regional factor of 4 (Chla_F4) for correcting the fluorescence-derived values, respectively (Roesler et al., 2017). The climatological mean \pm SD is shown for the Chla_F2 values as the green shaded area. Values obtained from the SOCLIM cruise sampling stations based on HPLC pigment analysis are indicated by the color-coded diamond symbols.

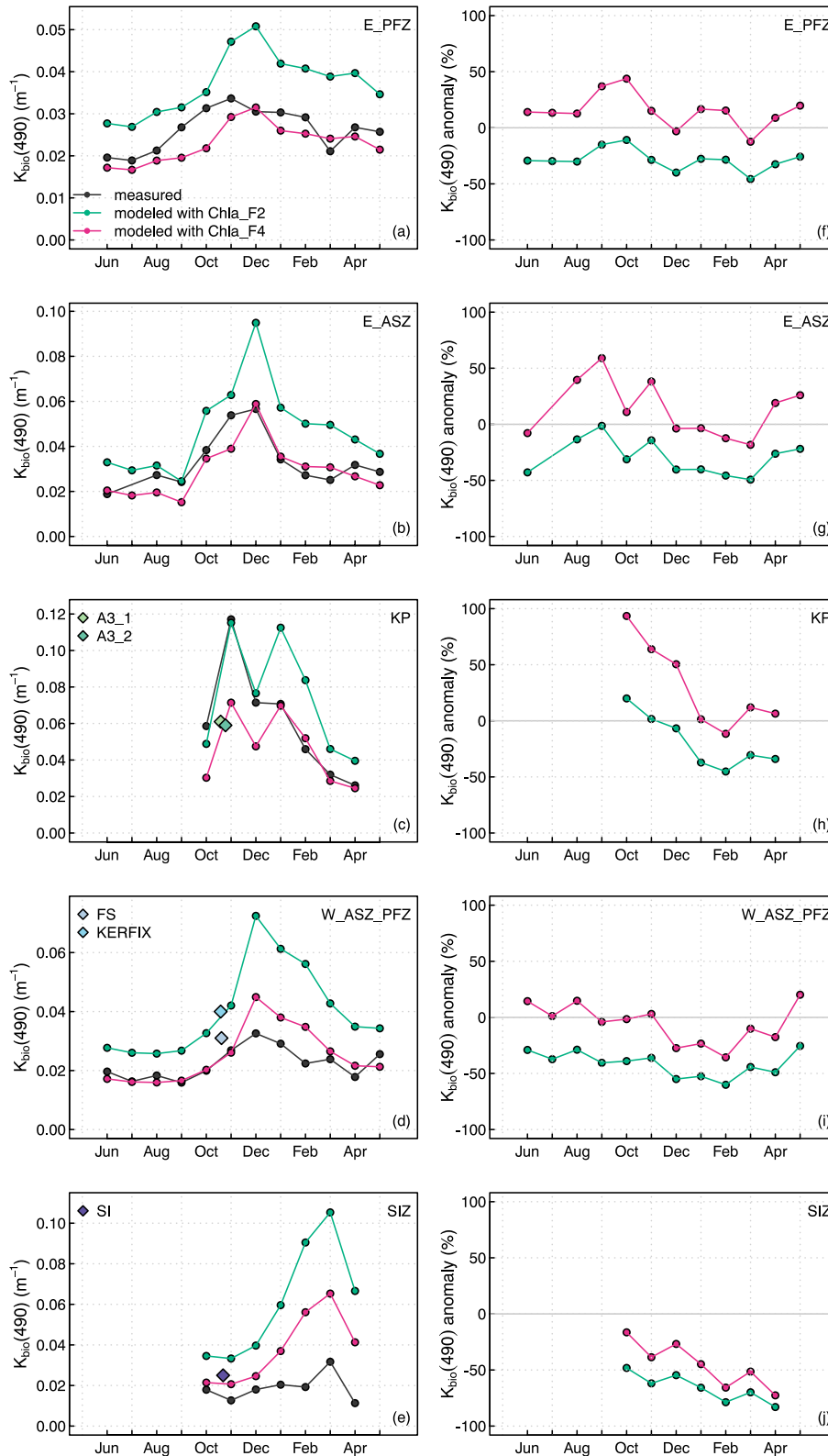


Figure 11.

minima coinciding with each of the two Chla peaks, indicating that for both Chla peaks $K_{\text{bio}}(490)$ may be affected by an increased contribution of large cells and/or photoacclimation to low light. However, the second peak shows higher PAR_{ML} values than the first one, suggesting more favorable light conditions in the mixed layer in January than in November. We may thus assume that the lower-than-predicted $K_{\text{bio}}(490)$ values observed in January may be mainly driven by a shift in the composition of the diatom assemblage from small diatoms in spring to large diatoms in summer, as reported by Blain et al. (2021) for the KP area. The larger sized population would, at comparable Chla levels, exhibit lower values of the absorption coefficient in the blue and, thus, of $K_{\text{bio}}(490)$.

Compared to the other regions, the SIZ stands out with measured $K_{\text{bio}}(490)$ significantly lower than predicted by the model of Morel and Maritorena (2001) during the entire bloom period covered by the float observations (Figures 11e and 11j). In this region, the anomaly index varies between -16% and -83% , which represents the largest degree of negative anomaly of all considered regions and seasons. This would suggest the summertime occurrence of large phytoplankton cells, that is, larger diatoms consistent with ice-edge blooms, and/or photoacclimation to low light. Both hypotheses are supported by very low $K_{\text{bio}}(490)/\text{Chla}$ values and moderate $b_{\text{bp}}(700)/\text{Chla}$ values (Figures 12e and 12j). Coinciding with the Chla peak, the PAR_{ML} suddenly drops to low levels, suggesting that the late bloom season could be associated with a $K_{\text{bio}}(490)$ anomaly largely driven by self-shading of phytoplankton cells (Figure 12o). We note, however, that our time series for the SIZ is limited to a period from spring to early fall, which unfortunately limits our ability to conclude on the behavior of the $K_{\text{bio}}(490)$ in the cold season (fall and winter).

Finally, we must consider that NAP and/or CDOM may contribute to absorption at 490 nm and thus affect the seasonal cycle of $K_{\text{bio}}(490)$ and the associated anomaly. Our complementary analysis of the absorption budget (Figure S4 in Supporting Information S1) indicates a limited contribution of NAP (14% – 24%) to $a(490)$ while that of CDOM is close to null. Therefore we can confidently use $K_{\text{bio}}(490)$ as a proxy for phytoplankton absorption in spring. Although this may change seasonally, the contribution of NAP to absorption generally covaries with Chla in the open ocean. Moreover, Bellacicco et al. (2019) reported that the fraction of NAP that does not covary with Chla makes a low contribution to the b_{bp} coefficient in the subpolar SO compared to the other regions and, seasonally, a larger contribution during the bloom season. Therefore, assuming that the NAP contribution to $K_{\text{bio}}(490)$ is non-negligible, it is unlikely to shift from low values in the high-biomass regimes observed in the spring and summer, to higher values in the low-biomass regimes in the fall and winter. Nevertheless, changes in the relative contribution of NAP to $K_{\text{bio}}(490)$ may also differ regionally in the SO. In particular, the relatively high $K_{\text{bio}}(490)$ anomalies in the KP zone might be partly attributed to the occurrence of absorbing NAP in the vicinity of the plateau. The broader amplitude of the seasonal cycle of the $K_{\text{bio}}(490)$ anomaly, which is observed for the zones under the influence of the plateau, could result from more pronounced seasonal changes not only in the composition and photoacclimation status of phytoplankton cells, but also in the absorption properties of NAP and its contribution to the total particle pool. Unfortunately, our data set does not allow us to explore this avenue further.

A comparison of the $K_{\text{bio}}(490)$ values derived from the BGC-Argo floats and the SOCLIM cruise calls for two comments. First, shipborne measurements indicate maximum anomalies of $a_{\text{ph}}(440)$ at stations TNS-06, TNS-08, and A3. In contrast, for the corresponding season and regions (E_ASZ and KP, respectively), the float-based measurements do not show large values of the anomaly index, which may be positive or negative depending on Chla_F2 or Chla_F4 being used as input to the model (Figures 11g and 11h). The float-based measurements in fact suggest that the anomaly index becomes negative and more pronounced as the bloom develops in summer. This seems coherent with a shift from a phytoplankton assemblage dominated by relatively small diatoms in spring to larger diatoms in summer in southern subpolar waters (Blain et al., 2021; Quéguiner, 2013) as well as with an increase in photoacclimation to low-light as a result of self-shading (Blain et al., 2013).

Figure 11. Monthly mean values of (a–e) the diffuse attenuation coefficient for downward irradiance at 490 nm, $K_{\text{bio}}(490)$ and (f–j) corresponding anomaly index for the five regions considered in this study: (a, f) the East Polar Front Zone, E_PFZ; (b, g) the East Antarctic Southern Zone, E_ASZ; (c, h) the Kerguelen Plateau, KP; (d, i) the West Polar Front Zone and West Antarctic Southern Zone, W_PFZ_ASZ; (e, j) the Seasonal Ice Zone, SIZ. For panels (a–e) the black curve represents the $K_{\text{bio}}(490)$ values retrieved from the radiometric measurements of the BGC-Argo floats, the green and pink curves show the $K_{\text{bio}}(490)$ values predicted from the general model of Morel and Maritorena (2001), using as input the monthly mean values of BGC-Argo-measured chlorophyll *a* concentration corrected with either a factor of 2 (Chla_F2) or a factor of 4 (Chla_F4), respectively. For panels (f–j), the anomaly index (in %) is calculated as the difference between the monthly mean of the measured $K_{\text{bio}}(490)$ values and the predictions from the model of Morel and Maritorena (2001), using as input either the monthly mean values of Chla_F2 (green curve) or Chla_F4 (pink curve), normalized to the predictions. Values derived from the SOCLIM cruise sampling stations using the model of Kirk (1991) are indicated by the color-coded diamond symbols.

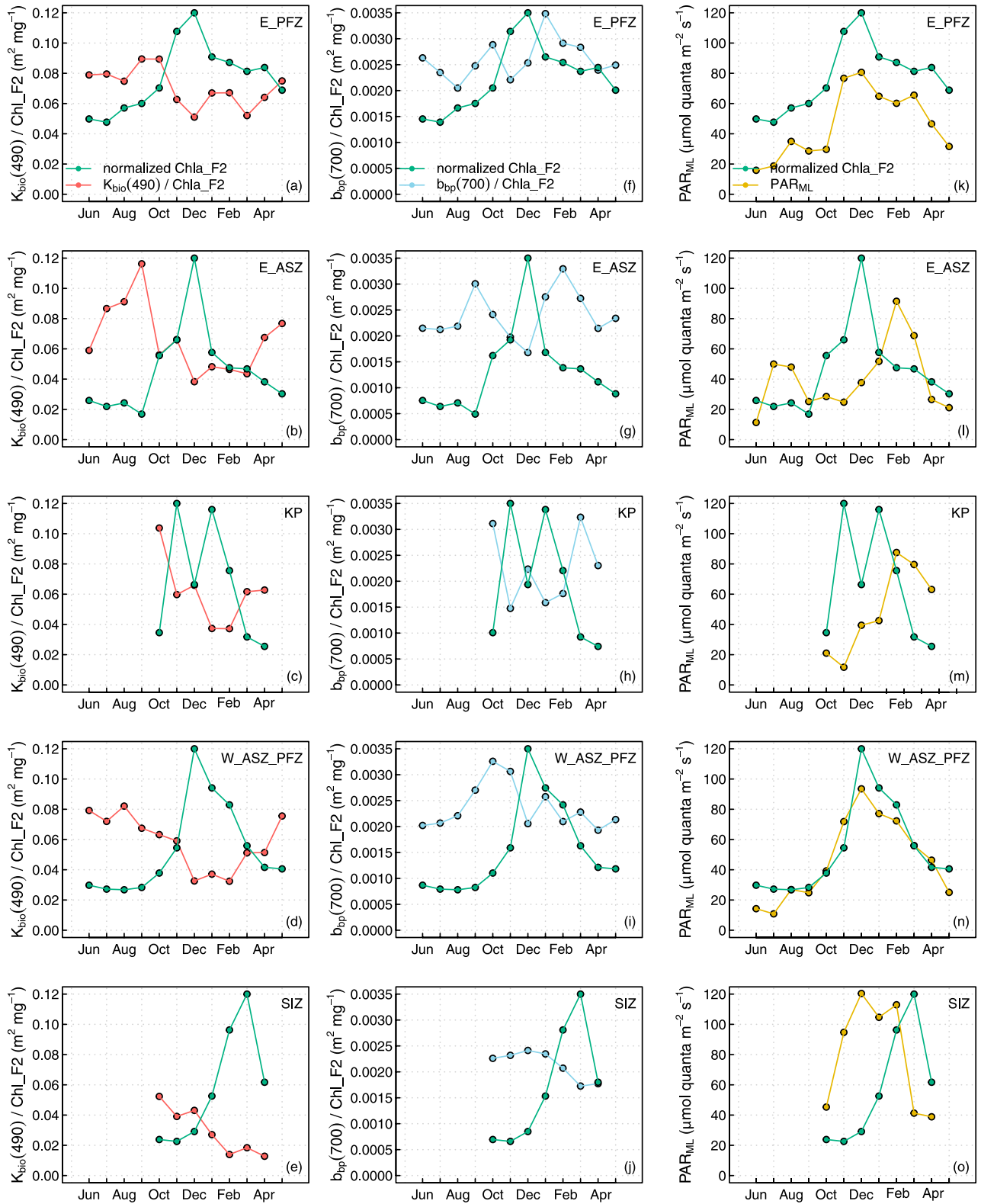


Figure 12.

Second, the shipborne data show that the anomaly in phytoplankton absorption in the blue is more pronounced in the iron-fertilized area. The float measurements, however, indicate that the HNLC (W_ASZ_PFZ) region, and even more so the SIZ, are also subject to substantial anomalies that vary seasonally and thus were not captured in the shipboard data (Figures 11i and 11j). Albeit shifted later in the season (maximum Chla in March; Figure 10e), the SIZ is characterized by a bloom as intense as that occurring in the waters under the influence of the KP (E_ASZ and KP; Figures 10b and 10c). Although future studies are needed to draw more robust conclusions, the SIZ summer bloom may well be dominated by large-sized phytoplankton cells like diatoms that may undergo photoacclimation in the second stage of the bloom, which would explain the strong anomaly in $K_{\text{bio}}(490)$ (Figures 11e and 11j). Previous studies conducted in a similar area ($\sim 60^\circ\text{S}$ in the open ocean) report a dominant contribution of micro-sized cells to the diatom population (Gomi et al., 2010) and, more generally, to the whole phytoplankton assemblage (Fiala et al., 2002; Rembauville et al., 2017).

The $K_{\text{bio}}(380)$ values derived from the BGC-Argo float measurements are used as a proxy for absorption by CDOM and NAP, following Organelli et al. (2017). The SOCLIM shipborne measurements indicate a lower than predicted contribution of NAP and CDOM to absorption at most stations (Figures 7c and 7e). In addition, the absorption budget at 380 nm (Figure S4 in Supporting Information S1) indicates a dominant contribution of CDOM (58%–71%), while those of NAP and phytoplankton are lower (14%–19% and 13%–25%, respectively). These observations, together with the fact that CDOM is generally the main contributor to the absorption coefficient at 380 nm (Bricaud et al., 2010), leads us to consider that, in our context, $K_{\text{bio}}(380)$ is a better proxy of $a_{\text{CDOM}}(380)$ than of $a_{\text{NAP}}(380)$. The $K_{\text{bio}}(380)$ coefficient derived from the float measurements varies seasonally in a manner consistent with Chla (Figure S5 in Supporting Information S1), which suggests that the production of CDOM is generally associated with autochthonous biological activity. The $K_{\text{bio}}(380)$ anomaly index shows a seasonal dynamic that is similar to that of $K_{\text{bio}}(490)$, with minimum, often negative, values during the apex of the bloom in all considered regions. This suggests that, in high Chla regimes, the contribution of CDOM is lower than predicted by the general model of Morel and Maritorena (2001). $K_{\text{bio}}(380)$ is also very low compared to the model predictions in the SIZ. Similar to $K_{\text{bio}}(490)$, the BGC-Argo observations of $K_{\text{bio}}(380)$ suggest that this pattern is not restricted to the waters under the influence of the KP but appears in the entire region with seasonal variations that become more pronounced as Chla increases.

As suggested by Organelli et al. (2017), the general relationship of Morel and Maritorena (2001) is biased toward subtropical and temperate environments and, thus, might fail to predict the behavior of both the $K_{\text{bio}}(380)$ and $K_{\text{bio}}(490)$ coefficients in the subpolar conditions encountered in the present study. This comment is also valid from a seasonal perspective, as the data on which the general relationship is based were typically collected in spring or summer, but very rarely (if ever) in winter or autumn. The general relationship used as a reference to identify the anomaly is therefore unlikely to represent the seasonal variability observed in the study region.

3.3.3. Particulate Backscattering Coefficient

The $b_{\text{bp}}(700)$ coefficient (Figures 13a–13e) measured by the BGC-Argo floats shows a mean seasonal cycle similar to that of Chla (Figure 10). The anomaly in $b_{\text{bp}}(700)$, determined using the global relationship of Barbieux et al. (2018) as reference, shows a reverse seasonal pattern compared to that of $K_{\text{bio}}(490)$ and $K_{\text{bio}}(380)$. Negative anomaly values are found in low Chla regimes (winter to fall), whereas high positive anomalies accompany the bloom season (spring to summer; Figures 13f–13j). The period of positive anomaly extends over summer or spring–summer depending on the region and use of Chl_F2 or Chl_F4 as input to the general model of Barbieux et al. (2018). This seasonal pattern applies to all regions apart from the KP zone. The KP does not seem to show a period of negative anomalies in the fall, although additional data from winter to fall would be needed to confirm this (Figures 13c and 13h). Finally, we note that the $b_{\text{bp}}(700)$ measurements show a much more pronounced seasonal amplitude than the predictions (i.e., the high values are higher while the low values are lower).

The $b_{\text{bp}}(700)$ measurements from the SOCLIM cruise are comparable to those from other open oceans with similar biomass levels. In contrast, the BGC-Argo float measurements show a more complex picture, with a

Figure 12. Monthly mean values of (a–e) the diffuse attenuation coefficient for downward irradiance at 490 nm, $K_{\text{bio}}(490)$, normalized to the chlorophyll *a* concentration; (f–j) the particulate backscattering coefficient at 700 nm, $b_{\text{bp}}(700)$, normalized to the chlorophyll *a* concentration; and (k–o) the mean photosynthetically available radiation in the mixed layer, PAR_{ML} , for the five regions considered in this study: (a) the East Polar Front Zone, E_PFZ; (b) the East Antarctic Southern Zone, E_ASZ; (c) the Kerguelen Plateau, KP; (d) the West Polar Front Zone and West Antarctic Southern Zone, W_PFZ_ASZ; (e) the Seasonal Ice Zone, SIZ. The chlorophyll *a* concentration used to normalize $K_{\text{bio}}(490)$ and $b_{\text{bp}}(700)$ was derived from the BGC-Argo float fluorescence measurements obtained using the global factor of 2 (Chla_F2, mg m^{-3}). On each panel the green curve represents the mean seasonal cycle of Chla_F2 shown in Figure 10 but normalized to its seasonal mean maximum (unitless).

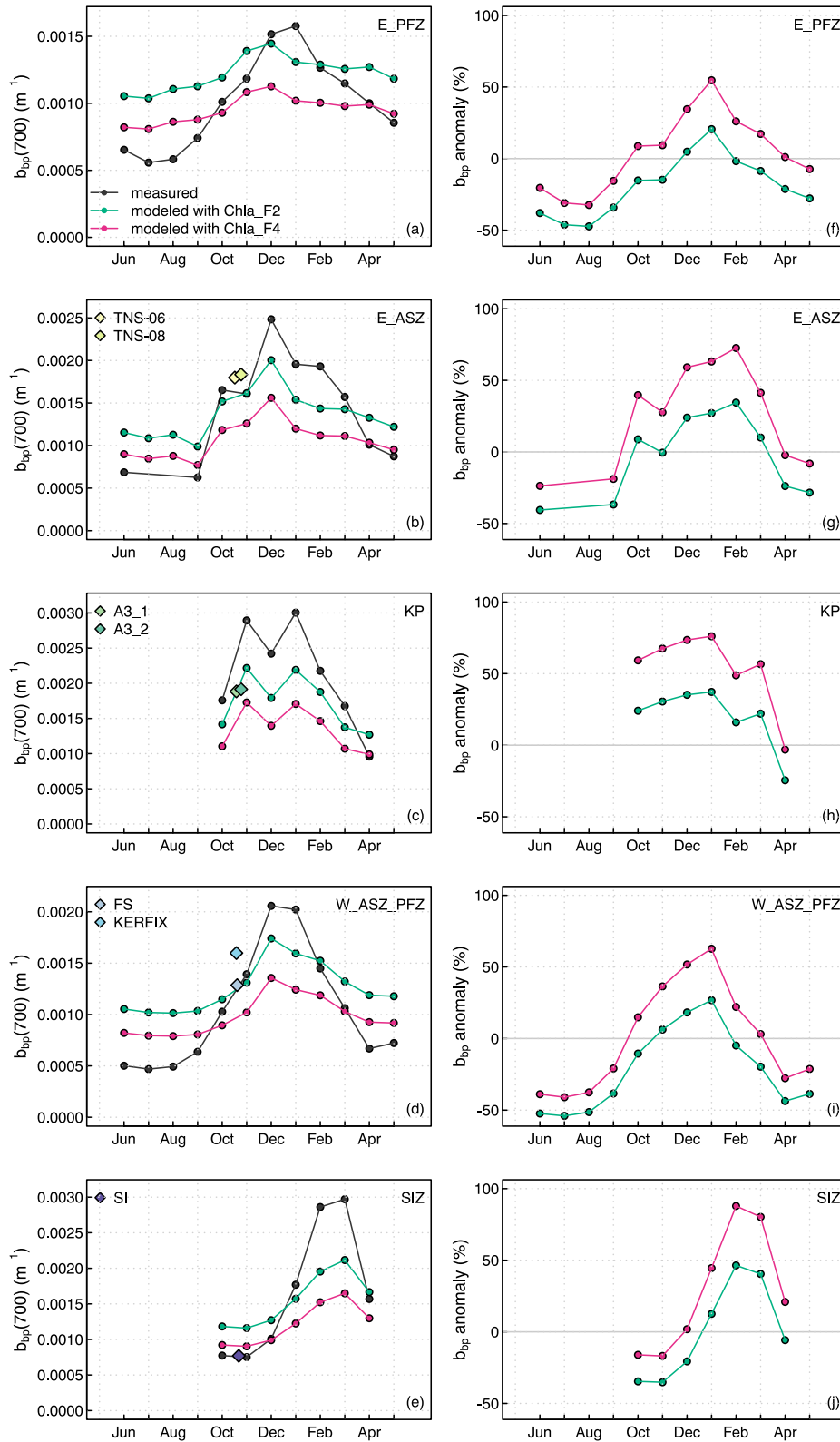


Figure 13.

marked seasonal pattern exhibiting large negative (positive) anomalies in low (high) biomass regimes. In other words, the slope of the $b_{bp}(700)$ -to-Chla relationship obtained from the float measurements (0.83 , $r^2 = 0.88$; not shown) is steeper than that derived from the SOCLIM cruise data set (0.32 , $r^2 = 0.77$; Table 3), consistent with $b_{bp}(700)$ -to-Chla relationships reported by Barbieux et al. (2018) for boreal and southern subpolar regions. Under low Chla conditions, the contribution of non-algal biogenic and mineral particles to $b_{bp}(700)$ may be lower in the study area than in other environments, consistently with previous studies (Bellacicco et al., 2019; Dierssen & Smith, 2000; Mitchell & Holm-Hansen, 1991a; Sosik et al., 1992). This may be explained in part because of the larger distance from terrestrial inputs and also due to tight trophic coupling. Lower than expected $b_{bp}(700)$ values in low biomass regimes of the SO can be explained by a reduced contribution to the particle pool of the small non-algal particles (e.g., detritus, bacteria) that are efficient backscatterers (Loisel et al., 2007; Stramski et al., 2004) and typically dominate low biomass regimes in other regions. A reduced contribution from small phytoplankton cells could not explain the low $b_{bp}(700)$ values, as picophytoplankton typically dominate southern subpolar waters in winter, consistently with the seasonal pattern of the $K_{bio}(490)$ anomaly and $K_{bio}(490)/Chla$ ratio (Section 3.3.2).

The positive anomaly observed in high Chla (bloom) conditions, suggests a transition in the composition and/or physiology of the phytoplankton assemblage, and/or a change in the nature of the non-algal particle pool. To consider the first option, that is, variations in the phytoplankton assemblage, the SOCLIM cruise measurements, as well as previous observations in summer (e.g., Lasbleiz et al., 2014; Uitz et al., 2009), typically indicate diatom dominance, a taxonomic group characterized by a relatively low backscattering coefficient (Stramski et al., 2001) and a low POC-to-Chla ratio (Sathyendranath et al., 2009). In the absence of other groups like coccolithophores, diatom variability cannot explain the observed anomalously high $b_{bp}(700)$ values under bloom conditions. We note, however, that Organelli et al. (2018), based on an optical model that takes into account the structural complexity of particles, reported higher b_{bp} coefficients than previously assumed from homogeneous sphere theory for phytoplankton cells of size $\sim 10 \mu\text{m}$. It is therefore not impossible that the presence of nano-sized diatoms in spring plays a role in the increase in $b_{bp}(700)$ at this time of the year.

In considering the likelihood of physiological changes driving the high $b_{bp}(700)$ values, the light-nutrient regime is also known as an important driver of the POC-to-Chla ratio in phytoplankton populations. Yet it is unlikely to explain the $b_{bp}(700)$ anomaly because the seasonal changes in $b_{bp}(700)$ anomaly is consistent among the different regions, in spite of their very different nutrient statuses (e.g., iron-fertilized vs. High Nutrient Low Chlorophyll) and the relatively low light conditions prevailing in the SO would act in the opposite direction (i.e., a decrease in the $b_{bp}(700)$ anomaly).

This leaves us with considering changes in the nature of the non-algal particulate pool. Bloom conditions in the SOCLIM region, which occurred after the sampling program, may generate more non-algal particles contributing to the $b_{bp}(700)$ signal than other systems with similar chlorophyll biomass. The study by Organelli et al. (2018, and reference herein) suggests that structural complexity in marine particles and aggregates would result in higher backscattering signal than the simple (homogeneous) particles that are generally considered. This result seems consistent with a hypothesis of a relatively high production of bloom by-products and may reflect in the $b_{bp}(700)/Chla$ maximum occurring 1–2 months after the Chla peak for most regions (Figure 12), which coincides with the maximum in the $b_{bp}(700)$ anomaly. If this is indeed the case, it suggests that there is a relatively inefficient transfer of particulate organic matter through the food web, leaving excess particulate organic matter in suspension for weeks to months.

4. Summary and Conclusion

The present study investigates the temporal, spatial, and depth variations in bio-optical relationships and regimes of open ocean waters of the Indian sector of the SO based on the analysis of two data sets. The first one was

Figure 13. Monthly mean values of (a–e) the particulate backscattering coefficient at 700 nm, $b_{bp}(700)$, and (f–j) corresponding anomaly index for the five regions considered in this study: (a, f) the East Polar Front Zone, E_PFZ; (b, g) the East Antarctic Southern Zone, E_ASZ; (c, h) the Kerguelen Plateau, KP; (d, i) the West Polar Front Zone and West Antarctic Southern Zone, W_PFZ_ASZ; (e, j) the Seasonal Ice Zone, SIZ. For panels (a–e) the black curve represents the $b_{bp}(700)$ values measured by the BGC-Argo floats, the green and pink curves show the $b_{bp}(700)$ values predicted from the general model of Barbieux et al. (2018), using as input the monthly mean values of BGC-Argo-measured chlorophyll *a* concentration corrected with either a factor of 2 (Chla_F2) or a factor of 4 (Chla_F4), respectively. For panels (f–j), the anomaly index (in %) is calculated as the difference between the monthly mean of the $b_{bp}(700)$ measurements and the predictions from the model of Barbieux et al. (2018), using as input either the monthly mean values of Chla_F2 (green curve) or Chla_F4 (pink curve), normalized to the predictions. Values derived from the surface SOCLIM cruise sampling stations are indicated by color coded diamond symbols.

acquired during the SOCLIM field cruise conducted in spring from subtropical oligotrophic waters, to the vicinity of Kerguelen Islands, and poleward to the edge of the SIZ. The second data set, collected by BGC-Argo floats deployed in the same region, provides insights into the seasonal and regional variability of the bio-optical properties, which nicely complements the shipborne biogeochemical and optical data.

The SOCLIM cruise stations, poleward of the oligotrophic stations, display a negative anomaly in the phytoplankton absorption coefficient in the blue waveband, $a_{ph}(440)$, which has significantly lower values compared to that in subtropical and temperate regions with comparable chlorophyll concentrations. This chlorophyll-specific phytoplankton absorption deficit is particularly pronounced in the naturally iron-fertilized area sampled downstream of Kerguelen. The cruise measurements highlight larger phytoplankton size as a driver of the negative $a_{ph}(440)$ anomaly, coupled with depth-independent photoacclimation over the respective mixed layers. Thus surface phytoplankton communities more resemble those acclimated to the lower light levels at depth and that is seen throughout the water column. Pigment composition covaries with these patterns. Specifically, the stations located both upstream (HNLC regime) and downstream (naturally iron-fertilized regime) of Kerguelen show atypically high fucoxanthin-to-chlorophyll ratios and low TAPs-to-chlorophyll ratios (true for each individual accessory pigment except fucoxanthin), suggesting a much larger contribution of diatoms to the phytoplankton assemblage in both the subpolar HNLC and iron-fertilized waters off Kerguelen than in other oceanic environments. The cruise measurements also indicate a relatively low contribution to absorption by CDOM and even less by NAP, in particular at the stations located downstream of Kerguelen, in comparison to other regions with similar chlorophyll levels.

The timing of the shipborne measurements was early spring, prior to regional blooms. This phase of seasonal ecosystem has been traditionally undersampled, but represents a larger portion of the annual cycle than does the bloom season, as revealed by the time course of observations provided by the BGC-Argo floats. Bio-optical proxy values measured onboard the ship compared well with those obtained by the floats at the time of the cruise. The float-based proxies, $K_{bio}(490)$ and $K_{bio}(380)$, likewise present low to negative anomaly during the pre-bloom season, but which becomes even more pronounced as the bloom develops in summer. The results suggest that changes in $K_{bio}(490)$ are largely driven by the combined effects of variations in phytoplankton composition/size and photoacclimation status. Coupled with information of light conditions, changes in $K_{bio}(490)$ might be used to monitor the shift from a phytoplankton assemblage dominated by relatively small diatoms in spring to larger diatoms in summer in southern subpolar waters or to identify spatial transitions in community structure. This may provide an alternative to the bio-optical index proposed by Cetinić et al. (2015). The BGC-Argo float-based K_{bio} proxies also show that the absorption anomaly is not restricted to the iron-fertilized area, as would be concluded from the sole cruise measurements, but is also observed in HNLC waters and in the SIZ where bio-optical investigations are very scarce.

In contrast to the absorption coefficients characterized by a significant anomaly, the SOCLIM cruise b_{bp} -to-chlorophyll relationship is comparable to the general model and reveals a strong coupling between b_{bp} and the phytoplankton biomass and covarying non-algal particles. Interestingly, the BGC-Argo float b_{bp} measurements exhibit a pronounced anomaly that varies seasonally, more than regionally. For most regions, the bloom conditions are associated with a positive b_{bp} anomaly whereas the low-biomass regimes are characterized by a negative anomaly. This pattern is attributed to a seasonally varying contribution of biogenic particles and trophic coupling.

The present study supports the remark of Organelli et al. (2017) that BGC-Argo floats are powerful tools to explore the variability in biogeochemical and optical properties beyond the relatively limited space and temporal scales covered by oceanographic cruises. We argue that, similar to its biogeochemical and phenological regimes (e.g., Ardyna et al., 2017; Thomalla et al., 2011; Uchida et al., 2019), the SO cannot be considered as a homogeneous system with respect to its bio-optical regime. Haëntjens et al. (2017) state that considering SO as a unique component leads to no deviation in general satellite ocean color algorithms, whereas examining small regional data set may introduce substantial bias compared to global relationship. This is consistent with our BGC-Argo float observations that reveal complex seasonal and regional patterns of the bio-optical regime, a conclusion that could not be derived from the sole SOCLIM cruise shipborne measurements.

Finally, we recommend pursuing investigations in order to improve the retrieval of the chlorophyll concentration from in situ fluorescence measurements (Petit et al., 2022; Roesler et al., 2017; Schallenberg et al., 2022). The uncertainty in the fluorescence-derived chlorophyll limits our ability to quantify the bio-optical anomaly of the

SO based on BGC-Argo float observations, although we are confident in the qualitative trend presented in this study.

Data Availability Statement

The BGC-Argo profiling float data were collected and made freely available by the International Argo Program (Argo, 2019) and the national programs that contribute to it (<https://argo.ucsd.edu>, <https://www.ocean-ops.org>). The Argo Program is part of the Global Ocean Observing System. The SOCLIM cruise data are available from the SEANOE database (Blain et al., 2022).

References

- Andrew, A. A., Del Vecchio, R., Subramaniam, A., & Blough, N. V. (2013). Chromophoric dissolved organic matter (CDOM) in the Equatorial Atlantic Ocean: Optical properties and their relation to CDOM structure and source. *Marine Chemistry*, *148*, 33–43. <https://doi.org/10.1016/j.marchem.2012.11.001>
- Aoki, S., Yamazaki, K., Hirano, D., Katsumata, K., Shimada, K., Kitade, Y., et al. (2020). Reversal of freshening trend of Antarctic bottom water in the Australian-Antarctic basin during 2010s. *Scientific Reports*, *10*(1), 14415. <https://doi.org/10.1038/s41598-020-71290-6>
- Ardyna, M., Claustre, H., Sallée, J.-B., D'Ovidio, F., Gentili, B., van Dijken, G., et al. (2017). Delineating environmental control of phytoplankton biomass and phenology in the Southern Ocean. *Geophysical Research Letters*, *44*(10), 5016–5024. <https://doi.org/10.1002/2016GL072428>
- Argo. (2019). Argo float data and metadata from global data assembly Centre (Argo GDAC)—Snapshot of Argo GDAC of July 8st 2019 [Dataset]. SEANOE. <https://doi.org/10.17882/42182#64916>
- Arrigo, K. R., Robinson, D. H., Worthen, D. L., Schieber, B., & Lizotte, M. P. (1998). Bio-optical properties of the southwestern Ross Sea. *Journal of Geophysical Research*, *103*(C10), 21683–21695. <https://doi.org/10.1029/98JC02157>
- Babin, M., Stramski, D., Ferrari, G. M., Claustre, H., Bricaud, A., Obolensky, G., & Hoepffner, N. (2003). Variations in the light absorption coefficients of phytoplankton, nonalgal particles, and dissolved organic matter in coastal waters around Europe. *Journal of Geophysical Research*, *108*(C7), 111579. <https://doi.org/10.1029/2001JC000882>
- Barbieux, M., Uitz, J., Bricaud, A., Organelli, E., Poteau, A., Schmechtig, C., et al. (2018). Assessing the variability in the relationship between the particulate backscattering coefficient and the chlorophyll a concentration from a global Biogeochemical-Argo database. *Journal of Geophysical Research: Oceans*, *123*(2), 1229–1250. <https://doi.org/10.1002/2017jc013030>
- Bellacicco, M., Cornec, M., Organelli, E., Brewin, R. J. W., Neukermans, G., Volpe, G., et al. (2019). Global variability of optical backscattering by non-algal particles from a Biogeochemical-Argo data set. *Geophysical Research Letters*, *46*(16), 9767–9776. <https://doi.org/10.1029/2019GL084078>
- Blain, S., Boutin, J., Claustre, H., Crispi, O., Debeljak, P., de Saint léger, E., et al. (2022). BIOGEOCHEMICAL dataset collected during the SOCLIM cruise [Dataset]. SEANOE. <https://doi.org/10.17882/71768>
- Blain, S., Quéguiner, B., Armand, L., Belviso, S., Bombled, B., Bopp, L., et al. (2007). Effect of natural iron fertilization on carbon sequestration in the Southern Ocean. *Nature*, *446*(7139), 1070–1075. <https://doi.org/10.1038/nature05700>
- Blain, S., Rembauville, M., Crispi, O., & Obernosterer, I. (2021). Synchronized autonomous sampling reveals coupled pulses of biomass and export of morphologically different diatoms in the Southern Ocean. *Limnology & Oceanography*, *66*(3), 753–764. <https://doi.org/10.1002/lno.11638>
- Blain, S., Renaut, S., Xing, X. G., Claustre, H., & Guinet, C. (2013). Instrumented elephant seals reveal the seasonality in chlorophyll and light-mixing regime in the iron-fertilized Southern Ocean. *Geophysical Research Letters*, *40*(24), 6368–6372. <https://doi.org/10.1002/2013gl058065>
- Böning, C. W., Dispert, A., Visbeck, M., Rintoul, S. R., & Schwarzkopf, F. U. (2008). The response of the Antarctic Circumpolar Current to recent climate change. *Nature Geoscience*, *1*(12), 864–869. <https://doi.org/10.1038/ngeo362>
- Boss, E., & Pegau, W. S. (2001). Relationship of light scattering at an angle in the backward direction to the backscattering coefficient. *Applied Optics*, *40*(30), 5503–5507. <https://doi.org/10.1364/AO.40.005503>
- Boyd, P. W. (2002). Environmental factors controlling phytoplankton processes in the Southern Ocean. *Journal of Phycology*, *38*(5), 844–861. <https://doi.org/10.1046/j.1529-8817.2002.t01-1-01203.x>
- Boyd, P. W., Doney, S. C., Strzepek, R., Dusenberry, J., Lindsay, K., & Fung, I. (2008). Climate-mediated changes to mixed-layer properties in the Southern Ocean: Assessing the phytoplankton response. *Biogeosciences*, *5*(3), 847–864. <https://doi.org/10.5194/bg-5-847-2008>
- Bricaud, A., Babin, M., Claustre, H., Ras, J., & Tieche, F. (2010). Light absorption properties and absorption budget of Southeast Pacific waters. *Journal of Geophysical Research*, *115*(C8), C08009. <https://doi.org/10.1029/2009jc005517>
- Bricaud, A., Babin, M., Morel, A., & Claustre, H. (1995). Variability in the chlorophyll-specific absorption coefficients of natural phytoplankton: Analysis and parameterization. *Journal of Geophysical Research*, *100*(C7), 13321–13332. <https://doi.org/10.1029/95JC00463>
- Bricaud, A., Claustre, H., Ras, J., & Oubelkheir, K. (2004). Natural variability of phytoplanktonic absorption in oceanic waters: Influence of the size structure of algal populations. *Journal of Geophysical Research*, *109*(C11), C11010. <https://doi.org/10.1029/2004jc002419>
- Bricaud, A., Morel, A., & Prieur, L. (1981). Absorption by dissolved organic matter of the sea (yellow substance) in the UV and visible domains. *Limnology & Oceanography*, *26*(1), 43–53. <https://doi.org/10.4319/lno.1981.26.1.0043>
- Bricaud, A., & Stramski, D. (1990). Spectral absorption coefficients of living phytoplankton and nonalgal biogenous matter: A comparison between the Peru upwelling area and the Sargasso Sea. *Limnology & Oceanography*, *35*(3), 562–582. <https://doi.org/10.4319/lno.1990.35.3.0562>
- Briggs, N., Perry, M. J., Cetinic, I., Lee, C., D'Asaro, E., Gray, A. M., & Rehm, E. (2011). High-resolution observations of aggregate flux during a sub-polar North Atlantic spring bloom. *Deep-Sea Research Part I*, *58*(10), 1031–1039. <https://doi.org/10.1016/j.dsr.2011.07.007>
- Brody, E., Mitchell, B. G., Holm-Hansen, O., & Vernet, M. (1992). RACER 3: Species-dependent variations of the absorption coefficient in the Gerlache Strait. *Antarctic Journal of the United States*, *27*(5), 160–162.
- Browning, T. J., Achterberg, E. P., Engel, A., & Mawji, E. (2021). Manganese co-limitation of phytoplankton growth and major nutrient draw-down in the Southern Ocean. *Nature Communications*, *12*(1), 884. <https://doi.org/10.1038/s41467-021-21122-6>
- Brunet, C., Johnsen, G., Lavaud, J., & Roy, S. (2011). Pigments and photoacclimation processes. In *Phytoplankton pigments: Characterization, chemotaxonomy and applications in oceanography*.
- Bushinsky, S. M., Landschützer, P., Rödenbeck, C., Gray, A. R., Baker, D., Mazloff, M. R., et al. (2019). Reassessing Southern Ocean air-sea CO₂ flux estimates with the addition of biogeochemical float observations. *Global Biogeochemical Cycles*, *33*(11), 1370–1388. <https://doi.org/10.1029/2019GB006176>

- Kramer, S. J., & Siegel, D. A. (2019). How can phytoplankton pigments be best used to characterize surface ocean phytoplankton groups for ocean color remote sensing algorithms? *Journal of Geophysical Research: Oceans*, *124*(11), 7557–7574. <https://doi.org/10.1029/2019JC015604>
- Kwiatkowski, L., Torres, O., Bopp, L., Aumont, O., Chamberlain, M., Christian, J. R., et al. (2020). Twenty-first century ocean warming, acidification, deoxygenation, and upper-ocean nutrient and primary production decline from CMIP6 model projections. *Biogeosciences*, *17*(13), 3439–3470. <https://doi.org/10.5194/bg-17-3439-2020>
- Landschützer, P., Gruber, N., Haumann, F. A., Rödenbeck, C., Bakker, D. C. E., van Heuven, S., et al. (2015). The reinvigoration of the Southern Ocean carbon sink. *Science*, *349*(6253), 1221–1224. <https://doi.org/10.1126/science.aab2620>
- Lasbleiz, M., Leblanc, K., Blain, S., Ras, J., Cornet-Barthaux, V., Hélias Nunige, S., & Quéguiner, B. (2014). Pigments, elemental composition (C, N, P, and Si), and stoichiometry of particulate matter in the naturally iron fertilized region of Kerguelen in the Southern Ocean. *Biogeosciences*, *11*(20), 5931–5955. <https://doi.org/10.5194/bg-11-5931-2014>
- Le Quéré, C., Takahashi, T., Buitenhuis, E. T., Rodenbeck, C., & Sutherland, S. C. (2010). Impact of climate change and variability on the global oceanic sink of CO₂. *Global Biogeochemical Cycles*, *24*(4), GB4007. <https://doi.org/10.1029/2009gb003599>
- Leung, S., Cabré, A., & Marinov, I. (2015). A latitudinally banded phytoplankton response to 21st century climate change in the Southern Ocean across the CMIP5 model suite. *Biogeosciences*, *12*(19), 5715–5734. <https://doi.org/10.5194/bg-12-5715-2015>
- Loisel, H., Mériaux, X., Berthon, J.-F., & Poteau, A. (2007). Investigation of the optical backscattering to scattering ratio of marine particles in relation to their biogeochemical composition in the eastern English Channel and southern North Sea. *Limnology & Oceanography*, *52*(2), 739–752. <https://doi.org/10.4319/lo.2007.52.2.0739>
- Lovenduski, N. S., Fay, A. R., & McKinley, G. A. (2015). Observing multidecadal trends in Southern Ocean CO₂ uptake: What can we learn from an ocean model? *Global Biogeochemical Cycles*, *29*(4), 416–426. <https://doi.org/10.1002/2014GB004933>
- Mannino, A., Novak, M. G., Nelson, N. B., Belz, M., Berthon, J. F., Blough, N. V., et al. (2019). Measurement protocol of absorption by chromophoric dissolved organic matter (CDOM) and other dissolved materials. In A. Mannino & M. G. Novak (Eds.), *Inherent optical property measurements and protocols: Absorption coefficient, IOCCG ocean optics and biogeochemistry protocols for satellite ocean colour sensor validation*. IOCCG.
- Matsuoka, A., Bricaud, A., Benner, R., Para, J., Sempéré, R., Prieur, L., et al. (2012). Tracing the transport of colored dissolved organic matter in water masses of the southern Beaufort sea: Relationship with hydrographic characteristics. *Biogeosciences*, *9*(3), 925–940. <https://doi.org/10.5194/bg-9-925-2012>
- Meijers, A. J. S. (2014). The Southern Ocean in the coupled model intercomparison project phase 5. *Philosophical Transaction of the Royal Society A*, *372*(2019), 20130296. <https://doi.org/10.1098/rsta.2013.0296>
- Mitchell, B. G. (1992). Predictive bio-optical relationships for polar oceans and marginal ice zones. *Journal of Marine Systems*, *3*(1), 91–105. [https://doi.org/10.1016/0924-7963\(92\)90032-4](https://doi.org/10.1016/0924-7963(92)90032-4)
- Mitchell, B. G., Brody, E. A., Holm-Hansen, O., McClain, C., & Bishop, J. (1991). Light limitation of phytoplankton biomass and macronutrient utilization in the Southern Ocean. *Limnology & Oceanography*, *36*(8), 1662–1677. <https://doi.org/10.4319/lo.1991.36.8.1662>
- Mitchell, B. G., & Holm-Hansen, O. (1991a). Bio-optical properties of Antarctic Peninsula waters: Differentiation from temperate ocean models. *Deep-Sea Research*, *38*(8–9), 1009–1028. [https://doi.org/10.1016/0198-0149\(91\)90094-v](https://doi.org/10.1016/0198-0149(91)90094-v)
- Mitchell, B. G., & Holm-Hansen, O. (1991b). Observations of modeling of the Antarctic phytoplankton crop in relation to mixing depth. *Deep-Sea Research, Part A: Oceanographic Research Papers*, *38*(8), 981–1007. [https://doi.org/10.1016/0198-0149\(91\)90093-U](https://doi.org/10.1016/0198-0149(91)90093-U)
- Morel, A., & Berthon, J.-F. (1989). Surface pigments, algal biomass profiles, and potential production of the euphotic layer: Relationships reinvestigated in view of remote-sensing applications. *Limnology & Oceanography*, *34*(8), 1545–1562. <https://doi.org/10.4319/lo.1989.34.8.1545>
- Morel, A., & Maritorena, S. (2001). Bio-optical properties of oceanic waters: A reappraisal. *Journal of Geophysical Research*, *106*(C4), 7163–7180. <https://doi.org/10.1029/2000jc000319>
- Moutier, W., Thomalla, S. J., Bernard, S., Wind, G., Ryan-Keogh, T. J., & Smith, M. E. (2019). Evaluation of chlorophyll-*a* and POC MODIS Aqua products in the Southern Ocean. *Remote Sensing*, *11*(15), 1793. <https://doi.org/10.3390/rs11151793>
- Nelson, N. B., & Siegel, D. A. (2013). The global distribution and dynamics of chromophoric dissolved organic matter. *Annual Review of Marine Science*, *5*(1), 447–476. <https://doi.org/10.1146/annurev-marine-120710-100751>
- Nelson, N. B., Siegel, D. A., & Michaels, A. F. (1998). Seasonal dynamics of colored dissolved material in the Sargasso Sea. *Deep Sea Research Part I: Oceanographic Research Papers*, *45*(6), 931–957. [https://doi.org/10.1016/S0967-0637\(97\)00106-4](https://doi.org/10.1016/S0967-0637(97)00106-4)
- Organelli, E., Bricaud, A., Antoine, D., & Matsuoka, A. (2014). Seasonal dynamics of light absorption by chromophoric dissolved organic matter (CDOM) in the NW Mediterranean Sea (BOUSSOLE site). *Deep Sea Research Part I: Oceanographic Research Papers*, *91*, 72–85. <https://doi.org/10.1016/j.dsr.2014.05.003>
- Organelli, E., & Claustre, H. (2019). Small phytoplankton shapes colored dissolved organic matter dynamics in the North Atlantic Subtropical Gyre. *Geophysical Research Letters*, *46*(21), 12183–12191. <https://doi.org/10.1029/2019GL084699>
- Organelli, E., Claustre, H., Bricaud, A., Barbieux, M., Uitz, J., D'Ortenzio, F., & Dall'Olmo, G. (2017). Bio-optical anomalies in the world's oceans: An investigation on the diffuse attenuation coefficients for downward irradiance derived from Biogeochemical Argo float measurements. *Journal of Geophysical Research: Oceans*, *122*(5), 3543–3564. <https://doi.org/10.1002/2016jc012629>
- Organelli, E., Claustre, H., Bricaud, A., Schmechtig, C., Poteau, A., Xing, X., et al. (2016). A novel near-real-time quality-control procedure for radiometric profiles measured by Bio-Argo floats: Protocols and performances. *Journal of Atmospheric and Oceanic Technology*, *33*(5), 937–951. <https://doi.org/10.1175/jtech-d-15-0193.1>
- Organelli, E., Dall'Olmo, G., Brewin, R. J. W., Tarran, G. A., Boss, E., & Bricaud, A. (2018). The open-ocean missing backscattering is in the structural complexity of particles. *Nature Communications*, *9*(1), 5439. <https://doi.org/10.1038/s41467-018-07814-6>
- Orsi, A. H., Whitworth, T., & Nowlin, W. D. (1995). On the meridional extent and fronts of the Antarctic Circumpolar Current. *Deep-Sea Research Part I*, *42*(5), 641–673. [https://doi.org/10.1016/0967-0637\(95\)00021-W](https://doi.org/10.1016/0967-0637(95)00021-W)
- Petit, F., Uitz, J., Schmechtig, C., Dimier, C., Ras, J., Poteau, A., et al. (2022). Influence of the phytoplankton community composition on the in situ fluorescence signal: Implication for an improved estimation of the chlorophyll-*a* concentration from BioGeoChemical-Argo profiling floats. *Frontiers in Marine Science*, *9*, 959131. <https://doi.org/10.3389/fmars.2022.959131>
- Polvani, L. M., Waugh, D. W., Correa, G. J. P., & Son, S.-W. (2011). Stratospheric ozone depletion: The main driver of twentieth-century atmospheric circulation changes in the Southern Hemisphere. *Journal of Climate*, *24*(3), 795–812. <https://doi.org/10.1175/2010jcli3772.1>
- Quéguiner, B. (2013). Iron fertilization and the structure of planktonic communities in high nutrient regions of the Southern Ocean. *Deep Sea Research Part II: Topical Studies in Oceanography*, *90*, 43–54. <https://doi.org/10.1016/j.dsr2.2012.07.024>
- Ras, J., Claustre, H., & Uitz, J. (2008). Spatial variability of phytoplankton pigment distributions in the subtropical South Pacific Ocean: Comparison between in situ and predicted data. *Biogeosciences*, *5*(2), 353–369. <https://doi.org/10.5194/bg-5-353-2008>

- Rembauville, M., Briggs, N., Ardyna, M., Uitz, J., Catala, P., Penkerch, C., et al. (2017). Plankton assemblage estimated with BGC-Argo floats in the Southern Ocean: Implications for seasonal successions and particle export. *Journal of Geophysical Research: Oceans*, *122*(10), 8278–8292. <https://doi.org/10.1002/2017jc013067>
- Reynolds, R. A., Matsuoka, A., Hirawake, T., Bélanger, S., & Mitchell, B. G. (2015). Ocean colour algorithms and bio-optical relationships for polar seas. In V. Stuart (Ed.) *Ocean colour remote sensing in polar seas* (pp. 61–94). International Ocean Color Coordinating Group (IOCCG).
- Reynolds, R. A., Stramski, D., & Mitchell, B. G. (2001). A chlorophyll-dependent semianalytical reflectance model derived from field measurements of absorption and backscattering coefficients within the Southern Ocean. *Journal of Geophysical Research*, *106*(C4), 7125–7138. <https://doi.org/10.1029/1999jc000311>
- Rintoul, S. R. (2007). Rapid freshening of Antarctic bottom water formed in the Indian and Pacific Oceans. *Geophysical Research Letters*, *34*(6), L06606. <https://doi.org/10.1029/2006GL028550>
- Rintoul, S. R. (2018). The global influence of localized dynamics in the Southern Ocean. *Nature*, *558*(7709), 209–218. <https://doi.org/10.1038/s41586-018-0182-3>
- Robinson, C. M., Huot, Y., Schuback, N., Ryan-Keogh, T. J., Thomalla, S. J., & Antoine, D. (2021). High latitude Southern Ocean phytoplankton have distinctive bio-optical properties. *Optics Express*, *29*(14), 21084–21112. <https://doi.org/10.1364/OE.426737>
- Roesler, C., Perry, M. J., & Carder, K. (1989). Modeling in situ phytoplankton absorption from total absorption spectra in productive inland waters. *Limnology & Oceanography*, *34*(8), 1510–1523. <https://doi.org/10.4319/lo.1989.34.8.1510>
- Roesler, C., Stramski, D., D'Sa, E. J., Röttgers, R., & Reynolds, R. A. (2018). Spectrophotometric measurements of particulate absorption using filter pads. In A. R. Neeley & A. Mannino (Eds.), *Ocean optics and biogeochemistry protocols for satellite ocean colour sensor validation, Volume 1.0 Inherent optical property measurements and protocols: Absorption coefficient*. International Ocean Colour Coordinating Group (IOCCG). <https://doi.org/10.25607/OBP-119>
- Roesler, C., Uitz, J., Claustre, H., Boss, E., Xing, X., Organelli, E., et al. (2017). Recommendations for obtaining unbiased chlorophyll estimates from in situ chlorophyll fluorometers: A global analysis of WET Labs ECO sensors. *Limnology and Oceanography: Methods*, *15*(6), 572–585. <https://doi.org/10.1002/lom3.10185>
- Sabine, C. L., Feely, R. A., Gruber, N., Key, R. M., Lee, K., Bullister, J. L., et al. (2004). The oceanic sink for anthropogenic CO₂. *Science*, *305*(5682), 367–371. <https://doi.org/10.1126/science.1097403>
- Sallée, J. B. (2018). Southern Ocean warming. *Oceanography*, *31*(2), 52–62. <https://doi.org/10.5670/oceanog.2018.215>
- Sallée, J.-B., Llorc, J., Tagliabue, A., & Lévy, M. (2015). Characterization of distinct bloom phenology regimes in the Southern Ocean. *ICES Journal of Marine Science*, *72*(6), 1985–1998. <https://doi.org/10.1093/icesjms/fsv069>
- Sallée, J. B., Pellichero, V., Akhondas, C., Pauthenet, E., Vignes, L., Schmidtke, S., et al. (2021). Summertime increases in upper-ocean stratification and mixed-layer depth. *Nature*, *591*(7851), 592–598. <https://doi.org/10.1038/s41586-021-03303-x>
- Sathyendranath, S., Lazzara, L., & Prieur, L. (1987). Variations in the spectral values of specific absorption of phytoplankton. *Limnology & Oceanography*, *32*(2), 403–415. <https://doi.org/10.4319/lo.1987.32.2.0403>
- Sathyendranath, S., Stuart, V., Nair, A., Oka, K., Nakane, T., Bouman, H., et al. (2009). Carbon-to-chlorophyll ratio and growth rate of phytoplankton in the sea. *Marine Ecology Progress Series*, *383*, 73–84. <https://doi.org/10.3354/meps07998>
- Schallenberg, C., Strzepek, R. F., Bestley, S., Wojtasiewicz, B., & Trull, T. W. (2022). Iron limitation drives the globally extreme fluorescence/chlorophyll ratios of the Southern Ocean. *Geophysical Research Letters*, *49*(12), e2021GL097616. <https://doi.org/10.1029/2021GL097616>
- Schmechtig, C., Poteau, A., Claustre, H., D'Ortenzio, F., & Boss, E. (2015). Processing Bio-Argo chlorophyll-*a* concentration at the DAC level (p. 12). IFREMER for Argo Data Management. <https://doi.org/10.13155/39468>
- Schmechtig, C., Poteau, A., Claustre, H., D'Ortenzio, F., Dall'Olmo, G., & Boss, E. (2018). Processing BGC-Argo particle backscattering at the DAC level. IFREMER for Argo Data Management (p. 15). <https://doi.org/10.13155/39459>
- Shindell, D. T., & Schmidt, G. A. (2004). Southern Hemisphere climate response to ozone changes and greenhouse gas increases. *Geophysical Research Letters*, *31*(18), L18209. <https://doi.org/10.1029/2004GL020724>
- Sosik, H. M., Vernet, M., & Mitchell, B. G. (1992). A comparison of particulate absorption properties between high- and mid-latitude surface water. *Antarctic Journal of the United States*, *27*, 162–164.
- Stewart, A. L., & Thompson, A. F. (2012). Sensitivity of the ocean's deep overturning circulation to easterly Antarctic winds. *Geophysical Research Letters*, *39*(18), L09606. <https://doi.org/10.1029/2012GL053099>
- Stramski, D., Boss, E., Bogucki, D., & Voss, K. J. (2004). The role of seawater constituents in light backscattering in the ocean. *Progress in Oceanography*, *61*(1), 27–56. <https://doi.org/10.1016/j.pocean.2004.07.001>
- Stramski, D., Bricaud, A., & Morel, A. (2001). Modeling the inherent optical properties of the ocean based on the detailed composition of the planktonic community. *Applied Optics*, *40*(18), 2929–2945. <https://doi.org/10.1364/AO.40.002929>
- Stramski, D., Reynolds, R. A., Kaczmarek, S., Uitz, J., & Zheng, G. M. (2015). Correction of pathlength amplification in the filter-pad technique for measurements of particulate absorption coefficient in the visible spectral region. *Applied Optics*, *54*(22), 6763–6782. <https://doi.org/10.1364/Ao.54.006763>
- Strzepek, R. F., Hunter, K. A., Frew, R. D., Harrison, P. J., & Boyd, P. W. (2012). Iron-light interactions differ in Southern Ocean phytoplankton. *Limnology & Oceanography*, *57*(4), 1182–1200. <https://doi.org/10.4319/lo.2012.57.4.1182>
- Sullivan, J. M., Twardowski, M. S., Zaneveld, J. R., & Moore, C. C. (2013). Measuring optical backscattering in water. In *Light scattering reviews* (Vol. 7, pp. 189–224). Springer. https://doi.org/10.1007/978-3-642-21907-8_6
- Szeto, M., Werdell, P. J., Moore, T. S., & Campbell, J. W. (2011). Are the world's oceans optically different? *Journal of Geophysical Research*, *116*(C7), 1323. <https://doi.org/10.1029/2011JC007230>
- Takahashi, T., Sweeney, C., Hales, B., Chipman, D. W., Newberger, T., Goddard, J. G., et al. (2012). The changing carbon cycle in the Southern Ocean. *Oceanography*, *25*(3), 26–37. <https://doi.org/10.5670/oceanog.2012.71>
- Thomalla, S. J., Fauchereau, N., Swart, S., & Monteiro, P. M. S. (2011). Regional scale characteristics of the seasonal cycle of chlorophyll in the Southern Ocean. *Biogeosciences*, *8*(10), 2849–2866. <https://doi.org/10.5194/bg-8-2849-2011>
- Trimborn, S., Thoms, S., Bischof, K., & Beszteri, S. (2019). Susceptibility of two Southern Ocean phytoplankton key species to iron limitation and high light. *Frontiers in Marine Science*, *6*, 167. <https://doi.org/10.3389/fmars.2019.00167>
- Uchida, T., Balwada, D., Abernathy, R., Prend, C. J., Boss, E., & Gille, S. T. (2019). Southern Ocean phytoplankton blooms observed by biogeochemical floats. *Journal of Geophysical Research: Oceans*, *124*(11), 7328–7343. <https://doi.org/10.1029/2019JC015355>
- Uitz, J., Claustre, H., Griffiths, F. B., Ras, J., Garcia, N., & Sandronic, V. (2009). A phytoplankton class-specific primary production model applied to the Kerguelen Islands region (Southern Ocean). *Deep-Sea Research Part I*, *56*(4), 541–560. <https://doi.org/10.1016/j.dsr.2008.11.006>
- Uitz, J., Claustre, H., Morel, A., & Hooker, S. B. (2006). Vertical distribution of phytoplankton communities in open ocean: An assessment based on surface chlorophyll. *Journal of Geophysical Research*, *111*(C8), CO8005. <https://doi.org/10.1029/2005jc003207>

- Uitz, J., Huot, Y., Bruyant, F., Babin, M., & Claustre, H. (2008). Relating phytoplankton photophysiological properties to community structure on large scales. *Limnology & Oceanography*, *53*(2), 614–630. <https://doi.org/10.4319/lo.2008.53.2.0614>
- Uitz, J., Stramski, D., Reynolds, R. A., & Dubranna, J. (2015). Assessing phytoplankton community composition from hyperspectral measurements of phytoplankton absorption coefficient and remote-sensing reflectance in open-ocean environments. *Remote Sensing of Environment*, *171*, 58–74. <https://doi.org/10.1016/j.rse.2015.09.027>
- Wong, A. P. S., Bindoff, N. L., & Church, J. A. (1999). Large-scale freshening of intermediate waters in the Pacific and Indian oceans. *Nature*, *400*(6743), 440–443. <https://doi.org/10.1038/22733>
- Xing, X., Claustre, H., Blain, S., D'Ortenzio, F., Antoine, D., Ras, J., & Guinet, C. (2012). Quenching correction for in vivo chlorophyll fluorescence acquired by autonomous platforms: A case study with instrumented elephant seals in the Kerguelen region (Southern Ocean). *Limnology and Oceanography: Methods*, *10*(7), 483–495. <https://doi.org/10.4319/lom.2012.10.483>
- Xing, X., Morel, A., Claustre, H., Antoine, D., D'Ortenzio, F., Poteau, A., & Mignot, A. (2011). Combined processing and mutual interpretation of radiometry and fluorimetry from autonomous profiling Bio-Argo floats: Chlorophyll a retrieval. *Journal of Geophysical Research*, *116*(C6), C06020. <https://doi.org/10.1029/2010JC006899>
- Yao, W., Shi, J., & Zhao, X. (2017). Freshening of Antarctic intermediate water in the South Atlantic Ocean in 2005–2014. *Ocean Science*, *13*(4), 521–530. <https://doi.org/10.5194/os-13-521-2017>
- Zhang, X., & Hu, L. (2009). Scattering by pure seawater at high salinity. *Optics Express*, *17*(15), 12685–12691. <https://doi.org/10.1364/OE.17.012685>

References From the Supporting Information

- Belzile, C., Vincent, W. F., & Kumagai, M. (2002). Contribution of absorption and scattering to the attenuation of UV and photosynthetically available radiation in Lake Biwa. *Limnology & Oceanography*, *1*, 95–107. <https://doi.org/10.4319/lo.2002.47.1.0095>
- Dall'Olmo, G., Westberry, T. K., Behrenfeld, M. J., Boss, E., & Slade, W. H. (2009). Significant contribution of large particles to optical backscattering in the open ocean. *Biogeosciences*, *6*, 947–967. <https://doi.org/10.5194/bg-6-947-2009>
- Pérez, G. L., Galf, M., Royer, S.-J., Sarmiento, H., Gasol, J. M., Marrasé, C., & Simó, R. (2016). Bio-optical characterization of offshore NW Mediterranean waters: CDOM contribution to the absorption budget and diffuse attenuation of downwelling irradiance. *Deep-Sea Research*, *114*, 111–127. <https://doi.org/10.1016/j.dsr.2016.05.011>
- Sullivan, J. M., Twardowski, M. S., Zaneveld, J. R. V., Moore, C. M., Barnard, A. H., Donaghay, P. L., & Rhoades, B. (2006). Hyperspectral temperature and salt dependencies of absorption by water and heavy water in the 400–750 nm spectral range. *Applied Optics*, *45*(21), 5294–5309. <https://doi.org/10.1364/AO.45.005294>
- Ulloa, O., Sathyendranath, S., & Platt, T. (1994). Effect of the particle-size distribution on the backscattering ratio in seawater. *Applied Optics*, *33*(30), 7070–7077. <https://doi.org/10.1364/AO.33.007070>
- Zaneveld, J. R. V., Kitchen, J. C., & Moore, C. M. (1994). The scattering error correction of reflecting-tube absorption meters. *Proceedings of SPIE*, *2258*, 44–55. <https://doi.org/10.1117/12.190095>